bioRxiv preprint doi: https://doi.org/10.1101/2022.03.17.484731; this version posted November 17, 2022. The copyright holder for this preprint (which was not certified by peer review) is the author/funder, who has granted bioRxiv a license to display the preprint in perpetuity. It is made available under aCC-BY 4.0 International license.

Mother cells control daughter cell proliferation in intestinal organoids to minimize proliferation fluctuations.

Guizela Huelsz-Prince[1], Rutger N.U. Kok[1], Yvonne J. Goos[1], Lotte Bruens[2], Xuan Zheng[1], Saskia I. Ellenbroek[2], Jacco van Rheenen[2], Sander J. Tans[1] , Jeroen S. van Zon[1,3]

[1]AMOLF, Science Park 104, 1098 XG, Amsterdam, The Netherlands

[2]Department of Molecular Pathology, Oncode Institute, Netherlands Cancer Institute, 1066 CX Amsterdam, the Netherlands.

[3]corresponding author

Abstract

During renewal of the intestine, cells are continuously generated by proliferation. Proliferation and differentiation must be tightly balanced, as any bias towards proliferation results in uncontrolled exponential growth. Yet, the inherently stochastic nature of cells raises the question how such fluctuations are limited. We used time-lapse microscopy to track all cells in crypts of growing mouse intestinal organoids for multiple generations, allowing full reconstruction of the underlying lineage dynamics in space and time. Proliferative behavior was highly symmetric between sister cells, with both sisters either jointly ceasing or continuing proliferation. Simulations revealed that such symmetric proliferative behavior minimizes cell number fluctuations, explaining our observation that proliferating cell number remained constant even as crypts increased in size considerably. Proliferative symmetry did not reflect positional symmetry, but rather lineage control through the mother cell. Our results indicate a concrete mechanism to balance proliferation and differentiation with minimal fluctuations, that may be broadly relevant for other tissues.

Keywords: stem cell dynamics; intestinal epithelium; homeostasis; fluctuations; cell proliferation; cell lineages; time-lapse microscopy; simulation

bioRxiv preprint doi: https://doi.org/10.1101/2022.03.17.484731; this version posted November 17, 2022. The copyright holder for this preprint (which was not certified by peer review) is the author/funder, who has granted bioRxiv a license to display the preprint in perpetuity. It is made available under aCC-BY 4.0 International license.

Introduction

Most adult organs and tissues constantly renew themselves by replacing old and damaged cells, while retaining their structure [1]. Theory indicates that this homeostasis requires a precise balance between proliferating and non-proliferating cells, as even a slight systematic bias towards producing proliferating cells yields uncontrolled exponential cell growth [2-7]. Moreover, the exponential nature of proliferation also readily amplifies fluctuations in the numbers of proliferating cells, which can lead to stochastic cell overgrowth or depletion in absence of additional control mechanisms [8,9]. How cell proliferation is balanced despite fluctuations has remained challenging to test in direct experiments, given the difficulties of following this process in time.

The mammalian intestine has become an important model system to study the mechanisms of tissue renewal and homeostasis[1,10]. The proliferating stem cells that sit at the base of intestinal crypts generate rapidly dividing transit-amplifying (TA) cells that in turn replenish the absorptive and secretory cells populating the lining of intestinal villi. Paneth cells positioned at the crypt bottom provide short-range signals that affect the proliferative and undifferentiated state of intestinal stem cells [11-13]. Originally, it was proposed that one or a few stem cells generated all differentiated cells by strictly asymmetric cell divisions [14,15], thus directly ensuring a constant stem cell pool. Subsequent studies rather suggested that individual cells stochastically and independently cease to divide or not[6,16,17]. In this 'population asymmetry' model, in principle one stem cell daughter could remain proliferative by staying adjacent to a Paneth cell, while the other daughter exits the stem cell niche, differentiates, and stops proliferating. However, such asymmetric outcome is no longer guaranteed. Instead, proliferation and differentiation are balanced more indirectly, by averaging these stochastic events across the total stem cell population.

Observations of neutral drift, in which the offspring of a single cell randomly take over the stem cell population of intestinal crypts [6,16,17] established the stochastic nature of stem cell proliferation that distinguishes the population asymmetry model from the earlier division asymmetry model. However, approaches used thus far do not follow the underlying cell divisions and lineages in time. Proliferation symmetry between sister cells and its role in homeostasis of the intestinal epithelium have so far only been inferred indirectly, typically by quantifying the clone size distributions at a certain time point. Hence, we also lack insight into the fluctuations in the number of proliferating cells and the mechanisms that control them.

Here, we developed an alternative approach: we employed time-lapse microscopy and single-cell tracking of all cells in crypts of mouse intestinal organoids [18], thus providing complete lineage trees, division dynamics, and cell movement, and combine it with mathematical modelling and intravital imaging of the mouse intestine. Surprisingly, we found that most cell divisions (>90%) were symmetric in proliferative outcome, producing daughter cells that either both continued to proliferate or both ceased proliferating. Proliferation was symmetric even when one daughter neighbored a Paneth cell, the source of proliferative signals in the crypt, while the other did not. Hence, proliferation was not independent between sisters, but rather controlled through the lineage by the mother. Our data and simulations explained not only how this behavior achieves homeostasis, but moreover, that it constitutes a near-optimal strategy to minimize fluctuations in the number of proliferating cells. Consistently, despite their large size increases over multiple generations in crypts of various size, the number of proliferating cells was notably constant in time and exhibited sub-

bioRxiv preprint doi: https://doi.org/10.1101/2022.03.17.484731; this version posted November 17, 2022. The copyright holder for this preprint (which was not certified by peer review) is the author/funder, who has granted bioRxiv a license to display the preprint in perpetuity. It is made available under aCC-BY 4.0 International license.

Poissonian fluctuations, indicating a precise balance between proliferative and non-proliferative sister pairs. Finally, by measuring clone size distributions in mice, we showed that stem cell divisions *in vivo* reproduced the strong symmetry in proliferative behavior between sister cells seen in organoids. As cell proliferation in many tissues follows inherently stochastic 'population asymmetry' mechanisms [3,16,19-21], we conjecture that high symmetry in proliferative behavior, controlled through the lineage, may be a more general mechanism to limit proliferation fluctuations.

Results

Single-cell tracking of complete crypts in growing intestinal organoids

To examine the dynamics of individual cells within crypts during growth, we used organoids with a H2B-mCherry nuclear reporter (**Figure 1A**) and performed confocal 3D time-lapse microscopy for up to 65 hours at a time resolution of 12 minutes. Cell division events were distinguished by the apical displacement of the mother cell nucleus, followed by chromosome condensation and separation, and finally, basal migration of the daughter cell nuclei (**Figure 1B**), consistent with epithelial divisions[22]. Custom-written software [23] was used to track every cell within organoid crypts by recording their nuclei positions in 3D space and time (**Figure 1C, Video 1**) and reconstruct lineage trees containing up to six generations (**Figure 1F**, **Figure 1-figure supplement 1**).

To study the cell lineages along the crypt surface, we 'unwrapped' the crypts: First, we annotated the crypt axes at every time point, then projected every cell position onto the surface of a corresponding cylinder, which we then unfolded (**Figure 1D,E**). This allowed us to visualize the cellular dynamics in a two-dimensional plane defined by two coordinates: the position along the axis and the angle around the axis. We found that lineages starting close to the crypt bottom typically continued to proliferate and expand in cell number, while those further up in the crypt contained cells that no longer divided during the experiment, consistent with stem cells being located at the crypt bottom and terminal differentiation occurring higher up along the crypt axis (**Figure 1F**). Lineages were also terminated by the death of cells, as observed by their extrusion into the lumen. This fate occurred more often in some lineages compared to others, and the frequency did not depend strongly on position along the crypt-villus axis. At the crypt bottom we also observed a small number of non-dividing cells, suggestive of terminally differentiated Paneth cells. Indeed, these cells typically exhibited the larger cell size and granules typical of Paneth cells. Finally, a small fraction of cells could not be tracked during the experiment, as they moved outside of the field of view, or their fluorescence signal was degraded due to scattering in the tissue.

Control of cell proliferation in organoid crypts

To systematically study proliferation control, we classified cells as proliferating when they divided during the experiment. Cells were classified as non-proliferating when they did not divide for >30 h or were born >60 μm away from the crypt bottom, as such cells rarely divided in our experiments (See **Materials and Methods** for details). A smaller fraction of cells could not be classified. Some cells were lost from tracking (7%, N=2880 cells). These cells were typically located in the villus region (**Figure 1F**) and therefore likely non-proliferating. For other cells, the experiment ended before a division could be observed or excluded based on the criteria above (27%). Such cases were

bioRxiv preprint doi: https://doi.org/10.1101/2022.03.17.484731; this version posted November 17, 2022. The copyright holder for this preprint (which was not certified by peer review) is the author/funder, who has granted bioRxiv a license to display the preprint in perpetuity. It is made available under aCC-BY 4.0 International license.

particularly prominent in the last 15 h of each time-lapse data set (22%). To analyze proliferation control, we therefore excluded all cells born <15 hr before the end of each experiment, thereby reducing the fraction of unclassified cells to 10%.

Using this classification procedure, we then quantified the total number of cells born in the tracked cell lineages for nine crypts and found a strong (~4-fold) increase in time (**Figure 2A)**. In contrast, the number of proliferating cells remained approximately constant in time for most crypts (**Figure 2B)**. Two crypts (crypt 3 and 4 in **Figure 2**) formed an exception with ~2-fold increase in the number of proliferating cells, an observation that we discuss further below. We then estimated the exponential growth rate α for each crypt, by fitting the dynamics of total number of cells born and proliferating cell number to a simple model of cell proliferation (discussed further below as the Uniform model), where proliferating cells divide randomly into proliferating and non-proliferating cells. In this model, the number of proliferating and non-proliferating cells increase on average by α and 1-α per cell division, respectively (**Materials and Methods**). Apart from Crypts 3 and 4, that displayed growth ($\alpha \approx 0.3$), the remaining crypts showed a low growth rate, $\alpha = 0.05 \pm 0.07$ (**Figure 2-figure supplement 1A-C**), indicating that birth of proliferating and non-proliferating cells was balanced on average. We then quantified the magnitude of fluctuations in the number of proliferating cells, N. Calculations of birth-death models of cell proliferation show that, without any control, the standard deviation of the proliferating cell number grows in time without bounds as $\sigma_D \sim \sqrt{Nt}$ [8]. In models without exponential growth, with proliferating cells born at constant rate, fluctuations are reduced: they are constant in time and Poissonian, $\sigma_D \sim \sqrt{N}$ [24]. In models where exponential growth was controlled by homeostatic feedback loops, fluctuations were further reduced to sub-Poissonian: $\sigma_D < \sqrt{N}$ [9]. Using the same measures, we found here that most crypts exhibited sub-Poissonian fluctuations (**Figure 2-figure supplement 1D**), implying the presence of a mechanism to limit fluctuations in proliferating cell number. Finally, we quantified the frequency of cell divisions along the crypt axis. Notably, divisions occurred in a region below 60 µm from the crypt base throughout the experiment, even as the crypts grew significantly (**Figure 2C**), indicating that the size of the proliferative region was constant in time. Moreover, the proliferative region was found to have a similar size in all analyzed crypts (**Figure 2D**), even though crypts varied both in size, as measured by diameter (30-50 µm, **Figure 2-figure supplement 1E**), and number of proliferating cells (**Figure 2B**). Overall, these results show that crypts by themselves are already capable of a specific form of homeostasis, namely maintaining a stationary number of proliferating cells that occupy a region of the crypt of constant size.

Symmetry of proliferative behavior between sister cells

To examine the origin of the observed balance between the birth of proliferating and non-proliferating cells, we first examined whether cell proliferation or cell death were correlated between sisters, for all observed sister pairs S_1 and S_2 (**Figure 3A**). Strikingly, we found that the decision to divide or not was highly symmetrical between sisters. In particular, occurrences where one sister divided but the other not were rare (2%) compared to cases where both divided or stopped dividing (74%). This correlation was also apparent by visual inspection of individual lineages, as sisters showed the same division behavior (**Figure 3B**, top). Indeed, if we ignore cell death, the fraction of pairs with symmetric proliferative outcome was high (97%) and could not be explained by sister cells making the decision to proliferate or not independently ($P<10^{-5}$, bootstrap simulation, **Materials and**

bioRxiv preprint doi: https://doi.org/10.1101/2022.03.17.484731; this version posted November 17, 2022. The copyright holder for this preprint (which was not certified by peer review) is the author/funder, who has granted bioRxiv a license to display the preprint in perpetuity. It is made available under aCC-BY 4.0 International license.

Methods). We also compared lineage dynamics between all cousin pairs C_1 and C_2 (**Figure 3A**). While we indeed found a significantly increased fraction (9%) of cousin pairs with asymmetrical division outcome, i.e. C_2 dividing and C_1 not, compared to sister pairs (2%), this fraction was still low, indicating that symmetric outcomes also dominated for cousins.

We found that symmetry between sisters did not only impact proliferation arrest, but also cell cycle duration: when a cell exhibited a longer-than-average cell cycle, this was typically mirrored by a similar lengthening of the cell cycle of its sister (**Figure 3B**, bottom). Indeed, cell cycle duration was strongly correlated between sisters (R=0.8, **Figure 3C**), even as cell cycle duration showed a broad distribution among tracked cells (**Figure 3–figure supplement 1**). In contrast, cell death was not symmetric between sisters, as the fraction of pairs where both cells died (9%) was smaller than the fraction of pairs where only a single sister died (14%, **Figure 3A**).

When examining all sister pairs in our data set, pairs of dividing sisters (59%) outnumber pairs of non-dividing sisters (15%), which appeared at odds with the observation that in most crypts the number of proliferating cells remain approximately constant (**Figure 2B**). This apparent mismatch was due to the exclusion of sister pairs where the proliferative state could not be classified in one sister or both (**Figure 3-figure supplement 2**), as the majority of these unclassified cells were likely non-proliferating. Indeed, when we restricted our sister pair analysis to the cells of crypts with $\alpha \approx 0$ in **Figure 2A,B** (Crypts 1,2,5,7-9) and furthermore assumed that all unclassified cells were non-proliferating, we found that now proliferating sister pairs (43%) are approximately balanced by non-proliferating sisters (40%, **Figure 3-figure supplement 2**).

Symmetry between sisters minimizes fluctuations in a cell proliferation model

In principle, any combination of (a)symmetric divisions would yield a constant number of proliferating cells on average, as long as the birth of proliferating and non-proliferating cells is balanced. We therefore hypothesized that the observed dominance of symmetric divisions might have a function specifically in controlling *fluctuations* in the number of proliferating cells. To test this hypothesis, we used mathematical modelling. Mathematical models of intestinal cell proliferation have been used to explain observed clone size statistics of stem cells [6,16,17,25], but so far not to examine the impact of division (a)symmetry on cell number fluctuations. We therefore examined simple stem cell models in which the degree of symmetry of sister cell proliferation could be tuned as an external parameter.

We first examined this in context of the canonical stochastic stem cell model[3], that we here refer to as the Uniform model. This model only considers cells as 'proliferating' or 'non-proliferating' (approximating stem and differentiated cells) and tissues that are unbounded in size, while ignoring spatial cell distributions. The parameter ϕ describes the division symmetry, with $\phi=1$ corresponding to purely symmetric divisions and $\phi=0$ to purely asymmetric divisions. The growth rate α describes the proliferation bias, with $\alpha>0$ indicating more proliferating daughters, and $\alpha<0$ more non-proliferating daughters on average. In our simulations, cells either divide symmetrically to produce two proliferating cells with probability $\frac{1}{2}(\phi+\alpha)$ or two non-proliferating cells with probability $\frac{1}{2}(\phi-\alpha)$, while the probability to divide asymmetrically is $1-\phi$ (**Figure 4A**). The number of proliferating cells

bioRxiv preprint doi: https://doi.org/10.1101/2022.03.17.484731; this version posted November 17, 2022. The copyright holder for this preprint (which was not certified by peer review) is the author/funder, who has granted bioRxiv a license to display the preprint in perpetuity. It is made available under aCC-BY 4.0 International license.

increases exponentially for $\alpha>0$ or decreases exponentially for $\alpha<0$ while homeostasis requires $\alpha=0$ [2,3] (**Figure 4B**).

When varying the division symmetry ϕ while maintaining α=0, we found that fluctuations in the number of proliferating cells N were minimized for ϕ=0 (**Figure 4B, C**), i.e. every division was asymmetric. In this scenario, the number of proliferating cells remains constant throughout each individual division by definition. Adding only a small fraction of symmetric divisions strongly increased the fluctuations in N. These fluctuations increased the risk of stochastic depletion, where all proliferating cells are lost, or uncontrolled increase in cell number, as previously observed in simulations [9], with the probability of such events occurring increasing with ϕ (**Figure 4B,C**). These trends are inconsistent with the symmetry between sisters we observed experimentally.

Hence, we extended the model by explicitly incorporating the observed subdivision of the crypt in a stem cell niche region, corresponding roughly to the stem cell niche, and a differentiation region, corresponding to the villus domain (**Figure 4D**). In the niche compartment, which has fixed size S, most divisions generate two proliferating daughter cells (α_n>0), while in the differentiation compartment, which has no size constraints, most divisions yield two non-proliferative daughters (α_d<0). Cell divisions in the niche compartment results in expulsion of the distalmost cell into the differentiation compartment, while neighboring cells swap positions in the niche compartment with rate r to include cell rearrangements. In contrast to the uniform model, where homeostasis only occurred for α=0, the compartment model shows homeostasis with $\alpha_{n,d}\neq 0$ in either compartment. Specifically, we found that the average number of proliferating cells in the two compartments, N_n and N_d, is given by $D_n = \alpha_n\, S$ and $N_d = S\ln(1+\alpha_n)\frac{\alpha_d-\alpha_n}{\alpha_d} - \alpha_n S$, independent of the division symmetry ϕ [26]. We simulated the proliferation dynamics for different values of α_n, α_d and ϕ (**Figure 4E,F**), where for simplicity we assumed the same ϕ in both compartments. For each combination of parameters, we varied the compartment size S so that $\langle N\rangle$=N_n+N_d=30, comparable to the number of proliferating cells per crypt in our experiments (**Materials and Methods, Figure 4-figure supplement 1A**). For cell rearrangements, we used $r\cdot T$=1, where T is the average cell cycle time, meaning that cells rearrange approximately once per cell cycle. For this r, our simulations reproduced the correlations in division outcome that we observed experimentally for cousins (**Figure 4-figure supplement 2A-C**), although we found that the dependence of the dynamics of N on the parameters ϕ, α_n and α_d did not depend strongly on r (**Figure 4-figure supplement 2D**).

By fixing $\langle N\rangle$, all simulations maintained the same number of proliferating cells on average, but potentially differed in the magnitude of fluctuations. Indeed, we found parameter combinations that generated strong fluctuations (**Figure 4E,F**, scenario 1) and stochastic depletion of all proliferating cells (scenario 2**).** Stochastic depletion occurred at significant rate (>1 event per 10^3 hours) when $\alpha_n \lesssim 0.5$ (**Figure 4-figure supplement 1B**) and implies that the existence of a stem cell niche, defined as a compartment with α>0, by itself does not guarantee homeostasis, unless its bias towards proliferation is high, $\alpha\approx 1$. For fixed α_d and α_n, we observed that fluctuations in N always decreased with more asymmetric divisions ($\phi\rightarrow 0$) (**Figure 4E,F**, scenarios 2,3), similar to the uniform model. However, the global fluctuation minimum was strikingly different (**Figure 4E,F**, scenario 4). Here, symmetric divisions dominated (ϕ=1), with all divisions generating two proliferative daughters in the niche compartment (α_n=1) and two non-proliferating daughters in the differentiation compartment (α_d=-1). Similar low fluctuations were found for a broader range of α_d, provided that $\alpha_n\approx 1$. When

bioRxiv preprint doi: https://doi.org/10.1101/2022.03.17.484731; this version posted November 17, 2022. The copyright holder for this preprint (which was not certified by peer review) is the author/funder, who has granted bioRxiv a license to display the preprint in perpetuity. It is made available under aCC-BY 4.0 International license.

we quantified the magnitude of fluctuations versus the average number of proliferating cells, we found that fluctuations for the suboptimal scenarios 1-3 were larger than those expected for a Poisson birth-death process (**Figure 2-figure supplement 1D**). In contrast, fluctuations in the optimal scenario 4 were similar to the low fluctuations we observed experimentally.

Our simulations also provided an intuitive explanation for this global minimum. A bias α_n=1 is only reached when the birth of non-proliferating cells in the niche compartment, by symmetric or asymmetric divisions, is fully avoided. In this limit, all cells in this compartment are proliferating, meaning that fluctuations in the niche compartment are entirely absent, with the only remaining fluctuations due to cells ejected from the niche compartment that subsequently divide in the differentiation compartment. Consistent with this explanation, we found that fluctuations in N increased when more symmetric divisions in the niche compartment generated non-proliferating daughters (scenarios 1 and 2). Finally, we note that the well-established neutral drift model of symmetrically dividing stem cells in a niche of fixed size [6,16] fails to reproduce the high symmetry in proliferation we experimentally observe between sister cells (**Figure 4-figure supplement 2E**), indicating that the size constraint of a niche is by itself not sufficient to generate this symmetry. In conclusion, our simulations show that the dominance of symmetric divisions we observed experimentally might function to minimize fluctuations in cell proliferation.

Symmetry of proliferation is independent of Paneth cell distance

Our results raised the question how the strong symmetry in proliferative behavior between sister cells is generated. Stem cell maintenance and cell proliferation is control by signals such as Wnt and EGF, that in organoids are locally produced by Paneth cells[12,27]. The symmetry between sister cells could therefore be explained by these sisters having a similar position relative to Paneth cells, leading them to experience a near identical environment in terms of proliferative signals. Alternatively, the proliferative behavior of sister cells could be controlled through the lineage, by their mother. In this case, symmetric proliferative behavior would even be seen in sisters that differ in position relative to Paneth cells. To differentiate between these two scenarios, we performed lysozyme staining after time-lapse imaging to retrospectively identify Paneth cells in our tracking data. Using crypt 'unwrapping' (**Figure 1D,E**), we calculated for each cell and each time point the link distance δ to the closest Paneth cell (**Materials and Methods, Figure 5-figure supplement 1A,B, Video 2**), i.e. the number of cells between the cell of interest and its closest Paneth cell, allowing us to examine proliferative behavior as function of distance to Paneth cells.

Paneth cell-derived Wnt ligands form gradients that only penetrate 1-2 cells into the surrounding tissue [27], suggesting that the steepest gradient in proliferative signals is found in close proximity to the Paneth cell. We therefore selected all dividing mother cells directly adjacent to a Paneth cell (δ_M=0) and examined their daughters. These sister pairs varied in Paneth cell distance ($\delta_{1,2}$≈0-2, **Figure 5A, Figure 5-figure supplement 1C**), with differences between sisters ($\delta_1 \neq \delta_2$) seen in 42% of pairs. We classified each sister pair as asymmetric in outcome, when only one sister continued proliferating, or symmetric (**Figure 5B**). In the latter case, we distinguished between symmetric pairs where both sisters divided and those were both stopped proliferating. We found that most daughters cells divided again, even though a small fraction ceased division even in close proximity to Paneth cells (**Figure 5B, Figure 5-figure supplement 1D**) However, whether cells divided or not was fully symmetric between sister pairs, even when one cell remained adjacent to a Paneth cell (δ_1=0)

bioRxiv preprint doi: https://doi.org/10.1101/2022.03.17.484731; this version posted November 17, 2022. The copyright holder for this preprint (which was not certified by peer review) is the author/funder, who has granted bioRxiv a license to display the preprint in perpetuity. It is made available under aCC-BY 4.0 International license.

while the other lost contact (δ_2>0). This also held for the few pairs where Paneth cell distance differed most between sisters (δ_1=0, δ_2=2).

When we instead examined mother cells that just lost contact with a Paneth cell (δ_M=1), we found that their offspring stopped proliferating more frequently (**Figure 5C**). While here we did find a substantial fraction of sister pairs with asymmetric outcome, for most pairs the outcome was still symmetric (92% of pairs), even for pairs that differed considerably in relative distance to the Paneth cell. Sister pairs with asymmetric outcome occurred more frequently for pairs with different Paneth cell distance ($\delta_1 \neq \delta_2$). For these pairs, however, the non-proliferating cell was the sister closest to the Paneth cell about as often as it was the more distant (5 and 3 pairs, respectively), indicating that position relative to the Paneth cell had little impact on each sister's proliferative behavior. Overall, these results show that the symmetry of proliferative behavior between sisters did not reflect an underlying symmetry in distance to Paneth cells, thus favoring a model where this symmetry is controlled by the mother cell.

Paneth cells control proliferative bias

Even though the proliferative behavior of sisters was not explained by their relative Paneth cell distance, we found that the bias towards proliferating daughters was clearly reduced when the Paneth cell distance of the mother increased (**Figure 5B,C**). Our simulations showed that both division symmetry and proliferative bias are important parameters in controlling fluctuations in the number of proliferating cells, with fluctuations minimized when most divisions are symmetric ($\phi \approx 1$), biased strongly towards producing two proliferating daughters in one compartment ($\alpha \approx 1$) and two non-proliferating daughters in the other ($\alpha \approx$-1). To compare our experiments against the model, we therefore measured the frequency of each division class as function of the mother's Paneth cell distance, averaging over all positions of the daughter cells (**Figure 5D**). Overall, cells had a broad range of Paneth cell distances (δ=0-10). Close to Paneth cells ($\delta \leq 1$), most divisions generated two proliferating daughters, while further away (δ>1), the majority yielded two non-proliferating cells. Asymmetry was rare and only occurred for δ=1-2. No divisions were seen for δ>5. When we used these measured frequencies to calculate α and ϕ as a function of Paneth cell distance (**Figure 5E**), we found good agreement with the parameter values that minimized fluctuations in the model, with a niche compartment of strong proliferation close to Paneth cells (α=0.67, $\delta \leq 1$) and a non-proliferative compartment beyond (α=-0.67), while almost all divisions were symmetric (ϕ=0.98).

The compartment model also predicted that the number of proliferating cells increases linearly with size S of the niche compartment. Above, we observed that the number of proliferating cells differed between crypts (**Figure 2B**). We therefore examined whether variation in number of proliferating cells between crypts could be explained by differences in Paneth cell number, in those crypts where we identified Paneth cells by lysozyme staining (Crypts 1-4). For the crypts that maintained a constant number of proliferating cells in time (Crypts 1-2), we found that differences in number of proliferating cells were well explained by differences in Paneth cell number. Moreover, in crypts with increasing number of proliferating cells (Crypts 3-4), we found that for Crypt 3 this change could be explained by an increase of Paneth cell number, due to cell divisions that generated Paneth cell sisters. In Crypt 4, however, proliferating cells increased in number without apparent Paneth cell proliferation. This crypt appeared to undergo crypt fission[28] at the end of the experiment, suggesting that during fission cell proliferation is altered without concomitant changes in Paneth cell

bioRxiv preprint doi: https://doi.org/10.1101/2022.03.17.484731; this version posted November 17, 2022. The copyright holder for this preprint (which was not certified by peer review) is the author/funder, who has granted bioRxiv a license to display the preprint in perpetuity. It is made available under aCC-BY 4.0 International license.

number. For Crypts 1-3, the relationship between number of proliferating and Paneth cells was well-fitted by a linear function (**Figure 5F**), consistent with the compartment model. The fitted slope of this line indicates that one Paneth cell maintains ~8 proliferating cells. This agrees with the observation in **Figure 5D** that divisions are strongly biased towards proliferation only for cells within the first and second ring of cells around each Paneth cell. Taken together, these results show that Paneth cells control proliferation by tuning the proliferative bias of divisions that are otherwise symmetric in proliferative outcome.

In vivo lineage tracing confirms symmetric proliferative behavior of sister cells

Finally, we asked whether the symmetry of proliferative behavior between sister cells was also observed in intestinal (stem) cells *in vivo*. Studying lineage dynamics with the high spatial and temporal resolution we employed here is currently impossible *in vivo*. However, we found that clone size distributions, which can be measured *in vivo*, exhibited a clear signature consistent with symmetric divisions. Specifically, clone size distributions of lineages generated by the compartment model showed that enrichment of even-sized clones depended strongly on a high frequency of symmetric divisions (**Figure 6A**). When we quantified clone size distributions for our organoid lineage data, by counting the number of progeny of each cell at the end of a 40 h time window, while sliding that window through our ~60 h data set, we indeed found that even clone sizes were strongly enriched compared to odd clone sizes (**Figure 6B**). Both for organoid and model data, we still observed odd clone sizes even when virtually all divisions were symmetric in proliferative behavior. This reflected variability in the cell cycle duration, with odd clone sizes typically resulting from symmetric divisions where one daughter had divided, but the other not yet.

To measure clone size distributions in the small intestine *in vivo*, we stochastically induced heritable tdTomato expression in Lgr5+ stem cells using *Lgr*5$^{\text{EGFP-ires-CreERT2}}$;R26$_{\text{LSL-tdTomato}}$ mice. We activated Cre-mediated recombination by tamoxifen and examined tdTomato expression after 60 hours, similar to the timescale of our organoid experiments, and imaged crypts with 3D confocal microscopy. Cre-activation occurred in one cell per ~10 crypts, indicating that all labeled cells within a crypt comprised a single clone. Indeed, we typically found a small number of tdTomato+ cells per crypt, of which most also expressed Lgr5-GFP (**Figure 6C**). We then counted the number of tdTomato+ cells per crypt to determine the clone size distribution and found a clear enrichment of even clone sizes (**Figure 6D**), with the overall shape of the distribution similar to that measured in organoids. Overall, these results indicated a dominant contribution of divisions with symmetric proliferative outcome also in the lineage dynamics of Lgr5+ stem cells *in vivo*.

Discussion

Self-renewing tissues exhibit homeostasis at multiple levels, such as overall tissue morphology, total cell number and the relative frequency of different cell types. To prevent exponential growth or tissue atrophy, the birth of each proliferating cell must be balanced by the loss of another through terminal differentiation. Experiments in a range of systems indicate that this is achieved through 'population asymmetry', with each cell making the decision to proliferate or not in a stochastic manner and this balance only achieved averaged over the entire population[1,3,16,20]. However, our

bioRxiv preprint doi: https://doi.org/10.1101/2022.03.17.484731; this version posted November 17, 2022. The copyright holder for this preprint (which was not certified by peer review) is the author/funder, who has granted bioRxiv a license to display the preprint in perpetuity. It is made available under aCC-BY 4.0 International license.

simulations showed that even though 'population asymmetry' ensures a constant pool of proliferating cells on average, its inherently stochastic nature can cause strong fluctuations in proliferating cell number, even resulting in their full depletion (**Figure 4**). This raises the question how these fluctuations are controlled.

We addressed this by a combined experimental and theoretical approach. We tracked all cell movements and divisions in the crypts of growing intestinal organoids, to reconstruct the full lineage of these crypts up to six generations (**Figure 1**). These data showed that the number of proliferating cells in most organoid crypts was approximately stationary, with small, i.e. sub-Poissonian fluctuations in their number, while non-proliferating cells were born at a constant rate (**Figure 2, Figure 2-figure supplement 1**), an indication of homeostatic control of cell proliferation that also limits fluctuations. That intestinal organoids exhibited homeostasis is notable, as organoid culture completely lacks surrounding tissue, such as the mesenchyme, that provides key signals regulating stem cell fate and proliferation[11,13], and shows that this form of homeostasis is inherent to the epithelium itself.

Our simulations showed that the fluctuations in proliferating cell number depended strongly on the relative proportion of divisions with symmetric proliferative outcome (either two proliferating or two non-proliferating daughters) and asymmetric outcome (one proliferating and one non-proliferating daughter), with small, sub-Poissonian cell number fluctuations only seen when most divisions had symmetric outcome (**Figure 4**, **Figure 2-figure supplement 1**). So far, the relative contribution of these three divisions patterns in the intestine could only be inferred indirectly from static measurements, leading to conflicting results[6,16,29,30]. Here, we used direct measurements of cell dynamics in time to unambiguously identify the proliferative state of successive generations of cells. These measurements show that virtually all cell divisions (>90%) showed symmetric proliferative behavior, generating either two proliferating or two non-proliferating sisters (**Figure 3**). Clone size distributions calculated based on our measured lineage data in organoids showed that this symmetry in proliferative behavior between sister cell gave rise to an enrichment of even clone sizes (**Figure 6**). Using short-term lineage tracing experiments in the mouse small intestine, we found that single Lgr5+ stem cells also gave rise to more even-sized than odd-sized clones, indicating that divisions that are symmetric in proliferative behavior indeed also dominate stem cell proliferation *in vivo*.

The symmetry in proliferative behavior we observe between sister cells could arise because both cells experience a highly similar environment, in terms of proliferative signals, or rather indicate control of cell proliferation through the lineage, by the mother cell. The current models of stem cell dynamics in the intestinal crypt favor a strong role for position relative to the stem cell niche, formed in organoids by Paneth cells, and a minor role, if any, for control of cell proliferation through the lineage[6,16,17]. We found that sister cells exhibited symmetric proliferative behavior, even when sisters differed in distance to Paneth cells (**Figure 5**), the sole source of proliferative Wnt signals in intestinal organoids[12]. This result implies control of proliferation by the mother cell rather than by each daughter's position in the stem cell niche. Our simulations provided a potential function for the predominance of divisions with symmetric proliferative outcome. When the tissue was subdivided into compartments of low and high cell proliferation, with the latter resembling the stem cell niche, we found that fluctuations in the number of proliferating cells were virtually eliminated, provided that cell divisions were symmetric, with all divisions generating two proliferating daughters in the niche compartment and two non-proliferating daughters outside (**Figure 4**). Consistently, in our

bioRxiv preprint doi: https://doi.org/10.1101/2022.03.17.484731; this version posted November 17, 2022. The copyright holder for this preprint (which was not certified by peer review) is the author/funder, who has granted bioRxiv a license to display the preprint in perpetuity. It is made available under aCC-BY 4.0 International license.

experiment we found that frequency of mother cells generating two proliferating rather than two non-proliferating daughters decreased with the mother's distance to the closest Paneth cell (**Figure 5**). Taken together, our results suggest a model where differences in proliferative behavior emerges in the cell lineage over at least two generations: while a mother cell division generates two daughters with the same proliferative behavior, these daughters might subsequently generate granddaughters that differ in proliferative behavior, depending on each daughter's position relative to the Paneth cells. This is consistent with our observation that the symmetry of proliferative behavior between cousins is reduced significantly compared to sisters (**Figure 3**).

We used mathematical modelling to explore the dependence of fluctuations in cell proliferation on the degree of symmetry in cell division outcome, arriving at a two-compartment model that matched key features of our experiments (**Figure 4D-F**). It reproduced the observed low, sub-Poissonian fluctuations in number of proliferating cells (**Figure 2-figure supplement 1D**), but only when division symmetry was high, as we also observed experimentally. In contrast, high symmetry increased fluctuations in a spatially uniform stem cell model (**Figure 4B,C**), while a standard neutral drift model of a stem cell niche[6,16] failed to reproduce the observed symmetry in outcome (**Figure 4-figure supplement 2**). Our model also reproduced the observed correlation in proliferative state between cousin cells (**Figure 4-figure supplement 2**), explaining it as arising from closely-related cells having similar location in the tissue and therefore similar probability of leaving the stem cell niche. Finally, it predicted the observed division of the tissue in a compartment where most divisions generated proliferating cells (close to Paneth cells) and one where divisions mostly generated non-proliferating daughters (away from Paneth cells) (**Figure 5**). However, the simplified nature of our model also poses limits. First, the observed transition from proliferating to non-proliferating daughter cells was more gradual than predicted by the model, indicating that each divisions proliferative outcome depended on space in a more complex manner than captured by the model. Second, the existence of compartments and the degree of symmetry in division outcome is imposed externally by the model rules. It will be interesting to examine whether simple mathematical models can explain how these properties emerge from the internal cellular states, long-range signaling pathways and local cell-cell interactions involved in intestinal homeostasis[1,10].

Precise control of cell proliferation is key to homeostasis. It has been proposed that cells may sense cell density, either by chemical signals or mechanical cues, and decrease cell proliferation (known as contact inhibition) if the cell number is too high [2,9,31], thereby ensuring homeostasis of and minimize fluctuations in the number of proliferating cells. Here, we provide a mechanism that achieves this without explicit sensing of cell density. Instead, it relies on the dominance of divisions symmetric in proliferative behavior of the daughter cells, coupled with the organization of a tissue in a proliferative niche (stem and transit amplifying cell) compartment, and a non-proliferative differentiation compartment. Such an organization is found widely, e.g. in the skin, hair follicles, testis among others [32]. In all these tissues, homeostasis of and minimizing fluctuations in the number of proliferating and differentiated cells must be essential. Hence, we speculate that the model we propose here, which exploits proliferative symmetry between sister cells to minimize fluctuations, is conserved more broadly and relevant to diverse tissue systems.

bioRxiv preprint doi: https://doi.org/10.1101/2022.03.17.484731; this version posted November 17, 2022. The copyright holder for this preprint (which was not certified by peer review) is the author/funder, who has granted bioRxiv a license to display the preprint in perpetuity. It is made available under aCC-BY 4.0 International license.

Figures

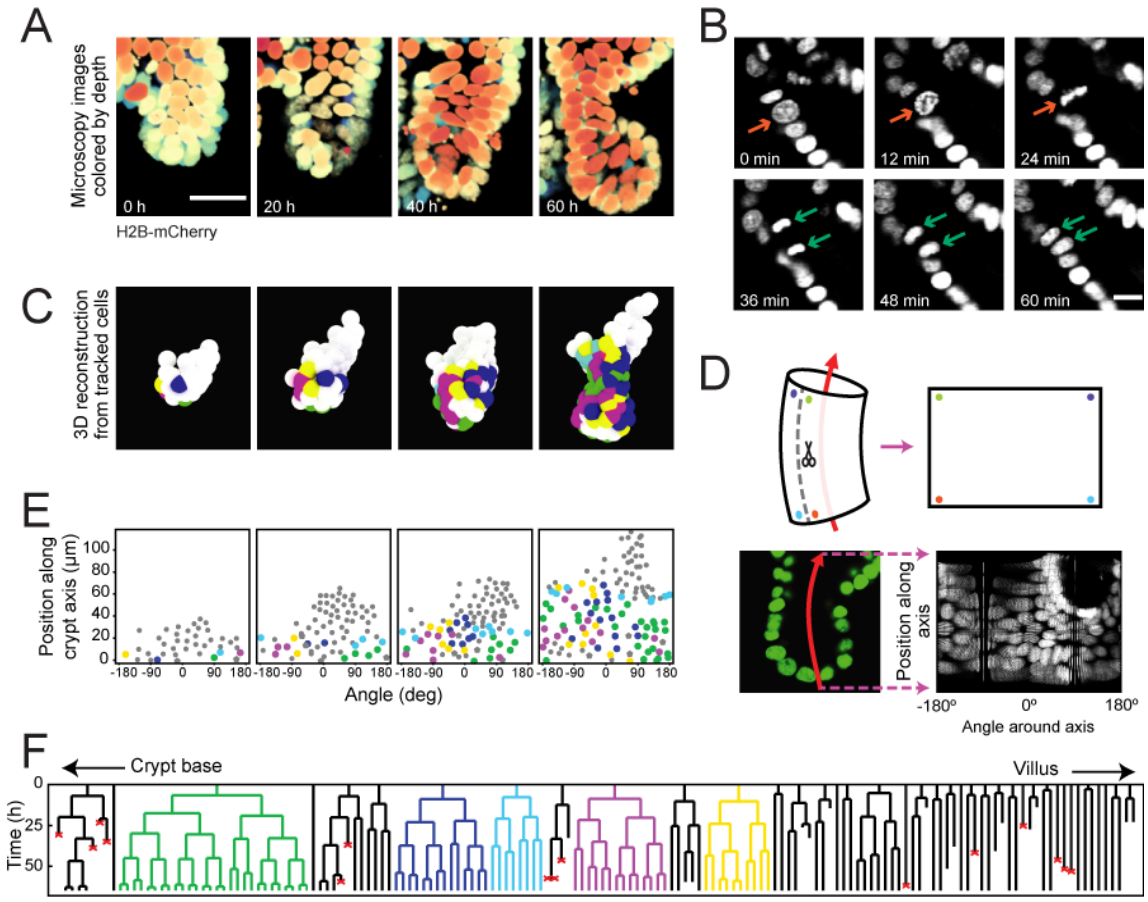

Figure 1. Time-lapse imaging and single-cell tracking of intestinal organoid crypts

(A) 3D reconstruction of an organoid expressing an H2B-mCherry reporter to visualize individual nuclei. Shown here is the crypt region, with nuclei colored by their depth along the optical axis. Scale bar is 25 µm. **(B)** Snapshots of a cell division event in a crypt. Cell divisions are distinguished by the apical migration of the nucleus followed by chromosome condensation (red arrows). After mitosis, the nuclei of the two newly born cells are displaced basally (green arrows). Scale bar is 10 µm. **(C)** 3D reconstruction of a crypt growing in time using the positions of tracked nuclei. Colors represent cells that belong to the same lineage. **(D)** Illustration of crypt unwrapping. After the crypt-villus axis is annotated (red arrow), tracked cell positions are projected onto the surface of a bent cylinder. The cylinder is then unfolded and its surface is mapped onto a two-dimensional plane defined by the distance along the axis and the angle around the axis. **(E)** Unwrapped representation of the crypt in (C), where colors represent the same lineages. **(F)** Lineage trees of cells within the crypt in (C) and colored accordingly. Cells in the initial time point are ordered according to their distance to the crypt base. Red crosses indicate cell deaths and incomplete lines indicate cells that could not be accurately traced further due to insufficient fluorescence intensity or movement outside of the field of view.

bioRxiv preprint doi: https://doi.org/10.1101/2022.03.17.484731; this version posted November 17, 2022. The copyright holder for this preprint (which was not certified by peer review) is the author/funder, who has granted bioRxiv a license to display the preprint in perpetuity. It is made available under aCC-BY 4.0 International license.

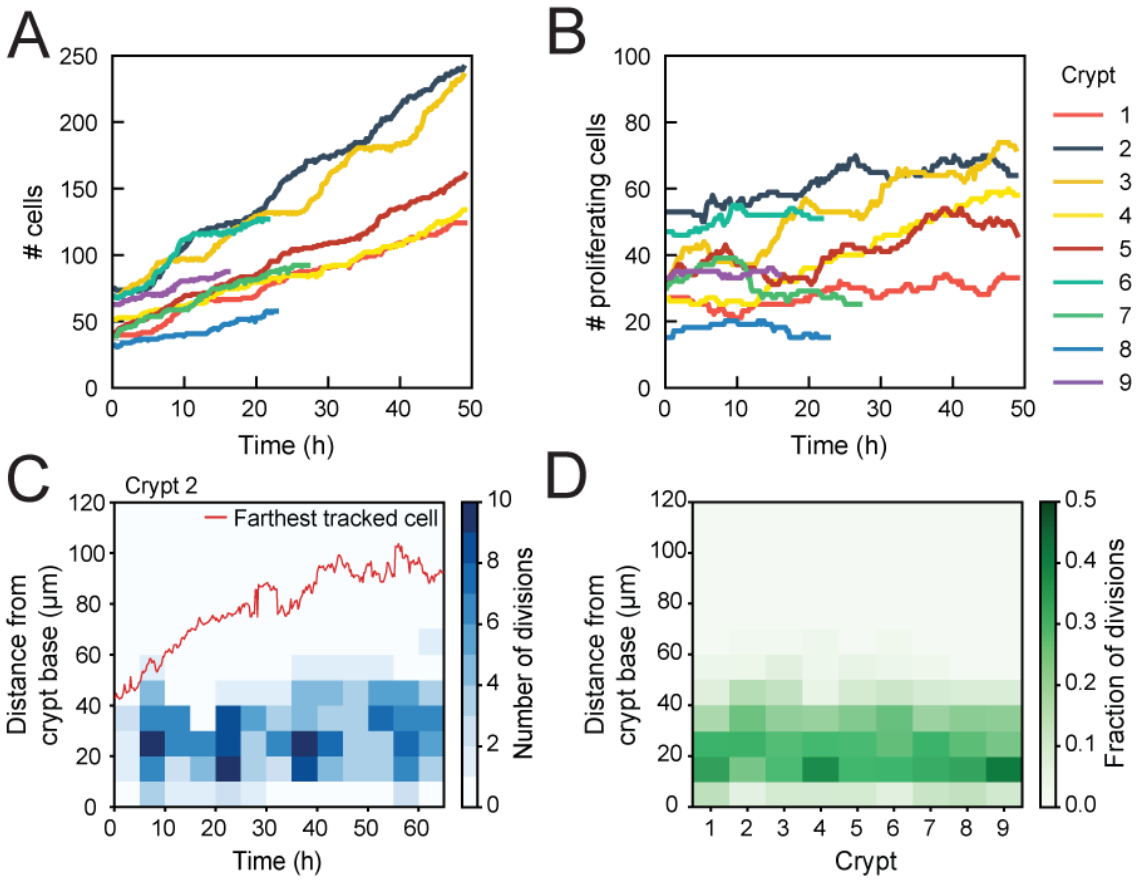

Figure 2. Control of cell divisions in intestinal organoids

(A) Total number of cells born and **(B)** number of proliferating cells as a function of time for all cell lineages followed in nine tracked crypts. Cells that died were classified as non-proliferating. Note the different scale along the y-axis. Whereas total cell number increases, the number of proliferating cells remains approximately constant. The strongest increase in number of proliferating cells (~2-fold) was seen in Crypts 3 and 4. **(C)** Number of divisions that occurred at different positions along the crypt axis as a function of time in a single tracked crypt. Red line corresponds to the position of the farthest tracked cell from the crypt base at every time point. Divisions occur in a compartment close to the crypt base, whose size remain constant over time. Apical displacement of the nuclei during mitosis results in few divisions occurring at less than 10 µm from the crypt base. **(D)** Fraction of divisions that occurred at different positions along the crypt axis for all tracked crypts, averaged over the full time course. The size of the proliferative region is similar between crypts, despite differences in the total number of divisions.

bioRxiv preprint doi: https://doi.org/10.1101/2022.03.17.484731; this version posted November 17, 2022. The copyright holder for this preprint (which was not certified by peer review) is the author/funder, who has granted bioRxiv a license to display the preprint in perpetuity. It is made available under aCC-BY 4.0 International license.

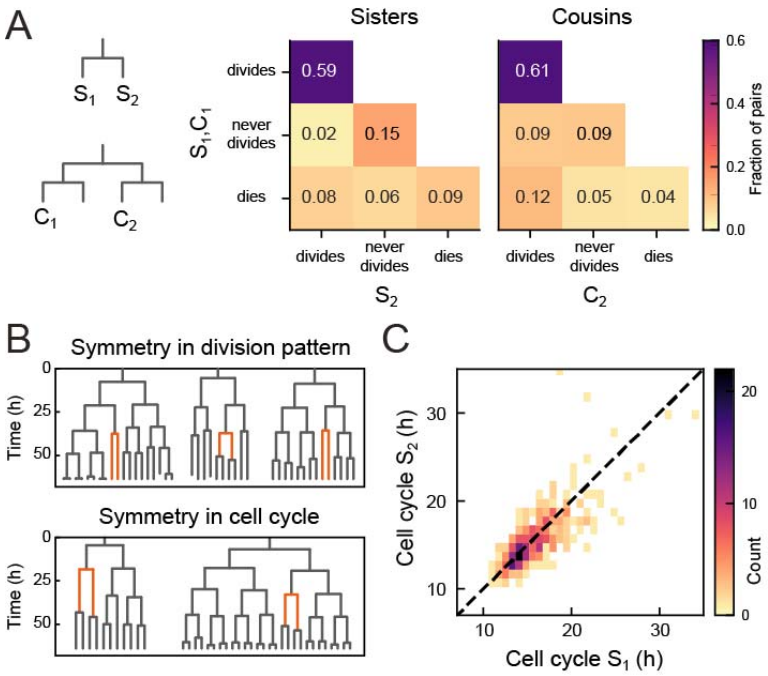

Figure 3. Symmetry of lineage dynamics between sister cells.

(A) Correlations in division patterns between sister (S_1,S_2) and cousin cells (C_1,C_2) (n=1004 and 1304 sister and cousin cell pairs). Most sister pairs show symmetrical outcomes, with most pairs consisting of sisters that either both divide or both cease dividing. Cell death occurs at low frequency and impacts sister cells asymmetrically. Symmetrical outcomes are still dominant for cousins, but the fraction of pairs that exhibited asymmetric proliferative outcomes (C_1 never divides, C_2 divides) was significantly increased in cousins compared to sisters ($P=2.4\cdot10^{-7}$, Pearson's Chi Square Test). **(B)** Representative examples of measured lineages highlighting pairs of sister cells (orange) that differ in lineage dynamics from their more distant relatives (black), either in terms of proliferative behavior (top) or cell cycle duration (bottom). **(C)** Duration of sister cell cycles plotted against each other for pairs in which both sisters divided. Cell cycle duration is strongly correlated between sisters (R=0.80).

bioRxiv preprint doi: https://doi.org/10.1101/2022.03.17.484731; this version posted November 17, 2022. The copyright holder for this preprint (which was not certified by peer review) is the author/funder, who has granted bioRxiv a license to display the preprint in perpetuity. It is made available under aCC-BY 4.0 International license.

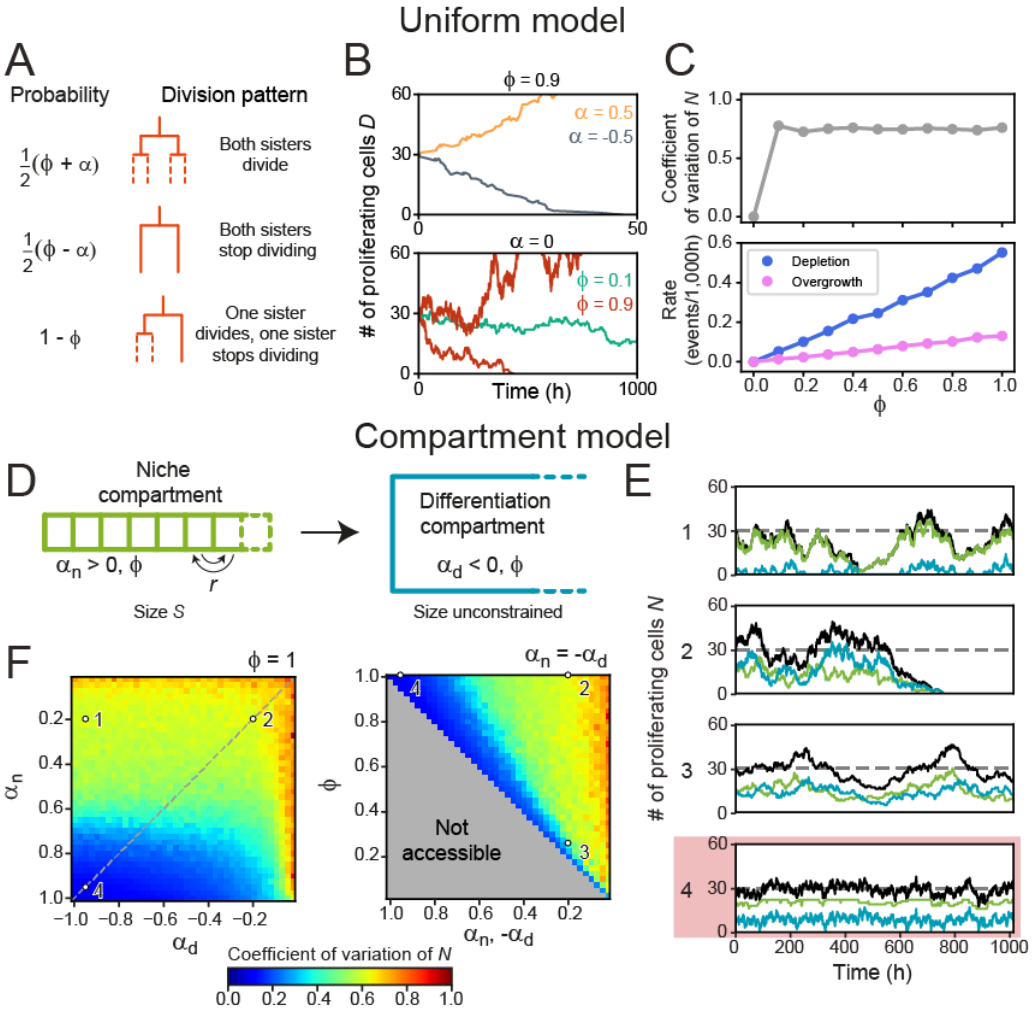

Figure 4. Cell number fluctuations in stem cell models.

(A) 'Uniform' stem cell model. The probability of each division pattern depends on α, the average increase in the number of proliferating cells per division, and ϕ, the fraction of divisions with symmetric outcome, while the total cell number is unconstrained **(B)** Number of proliferating cells, N, as function of time for different values of α (top) and ϕ (bottom). For $\alpha=0$, N remains constant on average, yet in this case fluctuations can cause stochastic depletion or overgrowth of proliferating cells, as shown for $\phi=0.9$ (bottom). **(C)** Coefficient of variation (standard deviation divided by mean) of N as a function of ϕ (top panel) and the probability of depletion ($N=0$, blue) or overgrowth ($N\geq$ 150, pink) events (bottom panel), for the 'Uniform' model with $\alpha=0$. Frequency of overgrowth depends strongly on the threshold value used. Fluctuations are minimal for $\phi=0$, i.e. only asymmetric divisions. **(D)** 'Compartment' model. Cells divide according to (A), but now the tissue is divided in a niche compartment n, with $\alpha_n>0$, and a differentiation compartment d, where $\alpha_d<0$. Both compartments have the same ϕ. In the niche compartment, the total number of cells cannot exceed S, so that upon cell division the distalmost cell (dashed square) moves into the differentiation compartment. Cells in the niche compartment switch positions at rate r. **(E)** Number of proliferating cells as a function of time in the niche (green) and differentiation compartment (blue). The total number of proliferating cells (black) fluctuates around the dashed line corresponding to $\langle N\rangle$. Each

bioRxiv preprint doi: https://doi.org/10.1101/2022.03.17.484731; this version posted November 17, 2022. The copyright holder for this preprint (which was not certified by peer review) is the author/funder, who has granted bioRxiv a license to display the preprint in perpetuity. It is made available under aCC-BY 4.0 International license.

panel's number refers to the parameter sets shown in (F). The parameter set with lowest fluctuations is outlined in red. **(F)** Coefficient of variation of N. Left panel shows the effects of varying the growth rates of both compartments when all divisions are symmetric ($\phi = 1$), and right panel of varying the degree of symmetry when both compartments have opposite growth rates (α_n=-α_d, dashed line in top panel). The grey region in bottom panel is inaccessible parameter space. Simulations ran with $\langle N \rangle$= 30, corresponding to our experimental observations, and rearrangements occurring approximately once per cell cycle. Fluctuations are minimized for α_n,-α_d=1 and ϕ=1, i.e. only symmetric divisions.

bioRxiv preprint doi: https://doi.org/10.1101/2022.03.17.484731; this version posted November 17, 2022. The copyright holder for this preprint (which was not certified by peer review) is the author/funder, who has granted bioRxiv a license to display the preprint in perpetuity. It is made available under aCC-BY 4.0 International license.

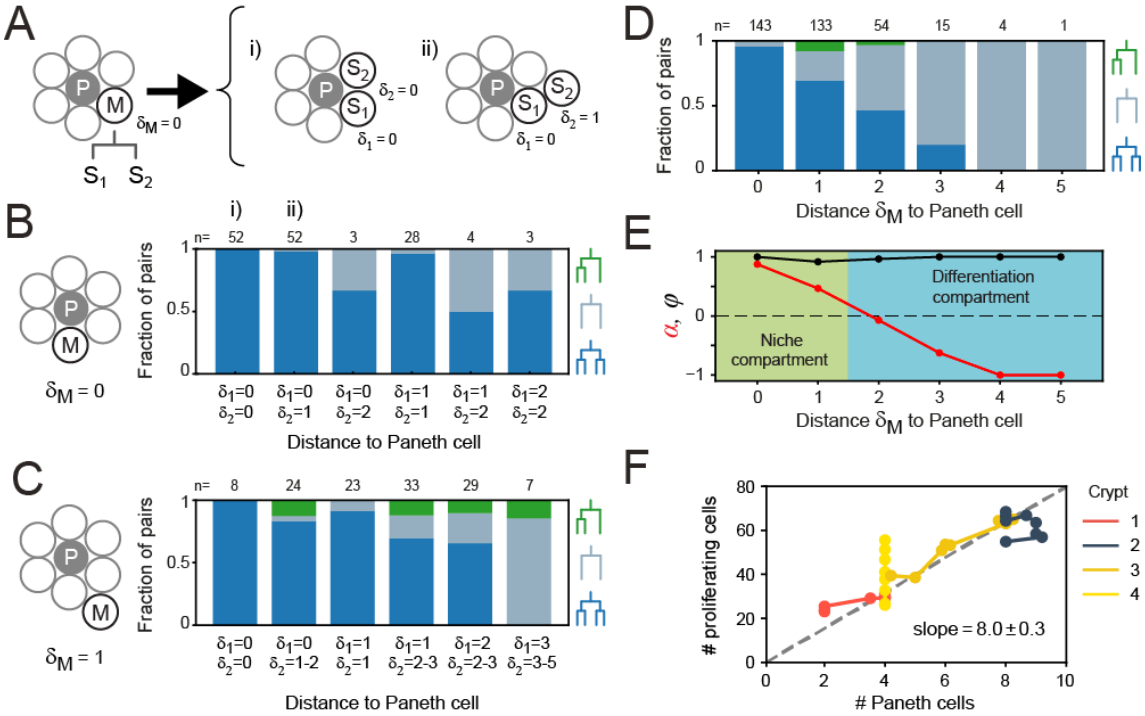

Figure 5. Impact of Paneth cell distance on proliferation.

(A) Dependence of proliferation on contact with Paneth cells. We examined cases where a mother cell (M) that touched a Paneth cell (P) divided into sister cells, S_1 and S_2, that either retained or lost Paneth cell contact. Here, the link distances δ_1 and δ_2 represents the number of cells between each sister and its closest Paneth cell. **(B)** Probability that both cells divide (blue), neither cell divides (orange) or only a single cell divides (green) for all sister pairs S_1 and S_2 of which the mother touched a Paneth cell (δ_M=0). Sister pairs exhibited full symmetry in proliferative behavior, even when distance to the Paneth cell differed between sisters ($\delta_1 \neq \delta_2$). **(C)** Same as (B) but for a mother cell positioned one cell away from the Paneth cell (δ_M=1). More daughter cells cease proliferation. While the fraction of pairs where only one sister divides increases, most sisters exhibit symmetric behavior. **(D)** Probability of each division pattern as function of Paneth cell distance of the mother cell. **(E)** Proliferative bias α and degree of symmetry ϕ as a function of Paneth cell distance. The observed values of α define a proliferative niche (green, $\alpha \approx 1$) and non-proliferative differentiation (blue, $\alpha < 0$) compartment, with the former corresponding approximately to the first two 'rings' of cells surrounding the Paneth cell. **(F)** Number of proliferating cells as function of Paneth cell number. Time-courses for individual crypts were divided into 5 hour intervals (markers), for which average cell numbers were calculated. Apart from Crypt 4, Paneth cell number correlated well with number of proliferating cells, even when Paneth cell number increased in time due to divisions. Dashed line is a linear fit to the data.

bioRxiv preprint doi: https://doi.org/10.1101/2022.03.17.484731; this version posted November 17, 2022. The copyright holder for this preprint (which was not certified by peer review) is the author/funder, who has granted bioRxiv a license to display the preprint in perpetuity. It is made available under aCC-BY 4.0 International license.

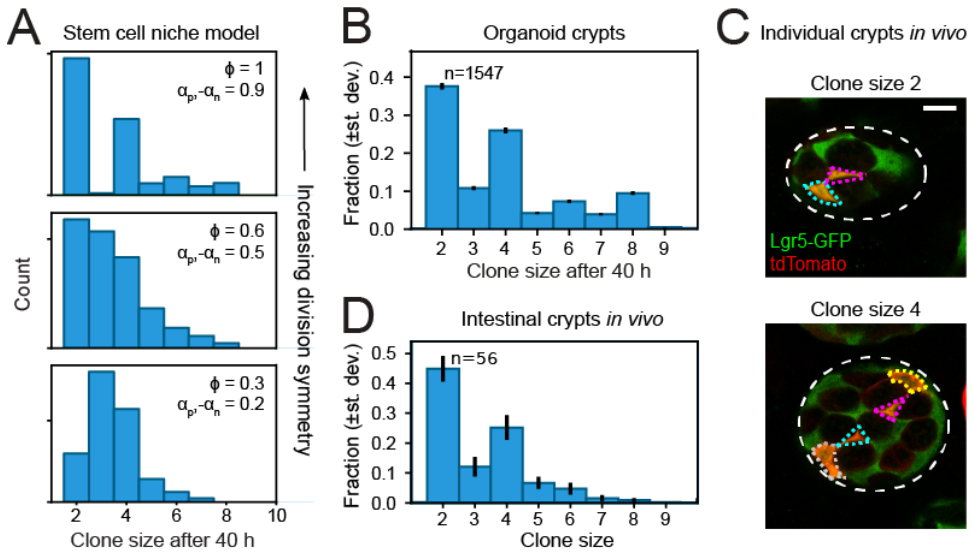

Figure 6. Clone size distributions reveal symmetry of proliferative behavior.

(A) Clone size distributions calculated for the Compartment model, for different degrees of division symmetry ϕ. Top panel corresponds to parameters that minimize fluctuations in number of proliferating cells. For high division symmetry, $\phi \approx 1$, even clone sizes are enriched compared to odd clone sizes. **(B)** Clone size distributions calculated for the lineage data obtained in organoids, for a sliding window of 40 h. Even clone sizes are enriched, consistent with the observed dominance of divisions with symmetric proliferative outcome. Error bars indicate standard deviation calculated using a bootstrapping approach (Materials and Method). **(C)** Examples of individual crypts found *in vivo,* displaying clone size 2 (top) and 4 (bottom). Crypts are viewed from the bottom, with individual cells belonging to a tdTomato+ clone (red) outlined. Scale bar is 10 µm. **(D)** Clone size distributions measured *in vivo* 60 h after induction of Cre-mediated recombination in small intestinal crypts of *Lgr*5$^{EGFP\text{-}ires\text{-}CreERT2}$;R26$_{LSL\text{-}tdTomato}$ mice (n=160 crypts). Even clone sizes 2 and 4 are enriched compared to odd clone sizes 3 and 5. Error bars indicate standard deviations calculated using a bootstrapping approach.

Supplementary Video 1. Tracking cell position and lineage.

(**Left**) 3D reconstruction of an organoid expressing an H2B-mCherry reporter to visualize individual nuclei. Shown here is the crypt region, with nuclei colored by their depth along the optical axis. (**Right**) 3D reconstruction of a crypt growing in time using the positions of tracked nuclei. Colors represent cells that belong to the same lineage.

Supplementary Video 2. Crypt unwrapping and Paneth cell distance

(Left) Unwrapped representation of the crypt in **Figure** 1, where colors represent the same lineages. **(Right)** Link distance δ of each cell to its closest Paneth cell. Pentagons indicate Paneth cells.

bioRxiv preprint doi: https://doi.org/10.1101/2022.03.17.484731; this version posted November 17, 2022. The copyright holder for this preprint (which was not certified by peer review) is the author/funder, who has granted bioRxiv a license to display the preprint in perpetuity. It is made available under aCC-BY 4.0 International license.

Materials and methods

Key resources table

Reagent type (species) or resource	Designation	Source or reference	Identifiers	Additional information
biological sample (Mus musculus)	H2B-mCherry (intestinal organoids)	Other	-	Gift from Hubrecht Institute, Clevers group
antibody	anti-lysozyme (polyclonal rabbit)	Dako	RRID:AB_2341230; Cat# A0099	IF(1:800)
antibody	anti-rabbit IgG H&L (Alexa Fluor® 405) (polyclonal donkey)	Abcam	RRID:AB_2715515; Cat# ab175649	IF(1:1000)
chemical compound, drug	Advanced DMEM/F-12 medium	Life Technologies	Cat# 12634010	-
other	Wheat Germ Agglutinin (WGA), CF®488A Conjugate	Biotium	Cat# 29022	5 µg/ml
other	RedDot™1 Far-Red Nuclear Stain	Biotium	Cat# 40060	1:200

Organoid culture

H2B-mCherry murine intestinal organoids were a gift from Norman Sachs and Joep Beumer (Hubrecht Institute, The Netherlands). Organoids were cultured in basement membrane extract (BME, Trevingen) and overlaid with growth medium consisting of murine recombinant epidermal growth factor (EGF 50 ng/ml, Life Technologies), murine recombinant Noggin (100 ng/ml, Peprotech), human recombinant R-spondin 1 (500 ng/ml, Peprotech), n-Acetylcysteine (1 mM, Sigma-Aldrich), N2 supplement (1x, Life Technologies) and B27 supplement (1x, Life Technologies), Glutamax (2 mM, Life Technologies), HEPES (10mM, Life Technologies), Penicilin/Streptomycin (100 U/ml 100 µg/ml, Life Technologies) in Advanced DMEM/F-12 (Life Technologies). Organoid passaging was performed by mechanically dissociating crypts using a narrowed glass pipette.

Time-lapse imaging

Mechanically dissociated organoids were seeded in imaging chambers one day before the start of the time-lapse experiments. Imaging was performed using a scanning confocal microscope (Nikon A1R MP) with a 40x oil immersion objective (NA = 1.30). 30 z-slices with 2 µm step size were taken per organoid every 12 minutes. Experiments were performed at 37°C and 5% CO_2. Small but already formed crypts that were budding perpendicularly to the objective were selected for imaging. Imaging data was collected for 3 independent experiments.

bioRxiv preprint doi: https://doi.org/10.1101/2022.03.17.484731; this version posted November 17, 2022. The copyright holder for this preprint (which was not certified by peer review) is the author/funder, who has granted bioRxiv a license to display the preprint in perpetuity. It is made available under aCC-BY 4.0 International license.

Fluorescent staining

After time-lapse imaging, organoids were fixed with 4% formaldehyde (Sigma) at room temperature for 30 minutes. Next, they were permeabilized with 0.2% Triton-X-100 (Sigma) for one hour at 4°C and blocked with 5% skim milk in TBS at room temperature for one hour. Subsequently, organoids were incubated in blocking buffer containing primary antibody (rabbit anti-lysozyme 1:800, Dako #A0099) overnight at 4°C, and then incubated with secondary antibody (anti-rabbit conjugated to Alexa Fluor©405 1:1,000, Abcam #ab175649) at room temperature for one hour. Afterwards, they were incubated with wheat germ agglutinin (WGA) conjugated to CF©488A (5 µg/ml Biotium) at room temperature for two hours, followed by incubation with RedDot™1 Far-Red Nuclear Stain (1:200, Biotium) at room temperature for 20 minutes. Finally, organoids were overlaid with mounting medium (Electron Microscopy Sciences). The procedure was performed in the same imaging chambers used for time-lapse imaging in order to maintain organoids in the same position. Imaging was performed with the same microscope as previously described. Note that WGA stains both Paneth and Goblet cells, but the lysozyme staining allowed the unequivocal distinction between them.

Single-cell tracking

Cells were manually tracked by following the center of mass of their nuclei in 3D space and time using custom-written image analysis software. Each cell was assigned a unique label at the start of the track. For every cell division, we noted the cell labels of the mother and two daughter cells, allowing us to reconstruct lineage trees. We started by tracking cells that were at the crypt bottom in the initial time point and progressively tracked cells positioned towards the villus region until we had covered all cells within the crypt that divided during the time-lapse recording. We then tracked at least one additional row of non-dividing cells positioned towards the villus region. Cell deaths were identified either by the extrusion of whole nuclei into the organoid lumen or by the disintegration of nuclei within the epithelial sheet. Only crypts that grew approximately perpendicularly to the imaging objective and that did not undergo crypt fission were tracked. During imaging, a fraction of cells could not be followed as they moved out of the microscope's field of view or moved so deep into the tissue that their fluorescence signal was no longer trackable. Because these cells were predominantly located in the villus region, where cells cease division, this likely resulted in underestimation of non-proliferating cells. Data was discarded when a large fraction (> 25%) of the cells in the crypt move out of the imaged volume.

Classifying cell state

To classify cells as either proliferating or non-proliferating, we followed the following procedure. Defining proliferating cells was straightforward, as their division could be directly observed. As for non-proliferating cells, we applied two criteria. First, cells were assigned as non-proliferating when they were tracked for at least 30 hours without dividing. This was based on our observation that cells cycle times longer than 30 hours were highly unlikely ($P=7.1\cdot10^{-7}$, from fit of skew normal distribution, **Figure 3-figure supplement 1**). However, we were not able to track all cells for at least 30 hours, as cells moved out of the field of view during the experiment or, more frequently, because they were born less than 30 hours before the end of the experiment. In this case, we defined a cell as non-proliferating if its last recorded position along the crypt axis was higher than 60 µm, as almost

bioRxiv preprint doi: https://doi.org/10.1101/2022.03.17.484731; this version posted November 17, 2022. The copyright holder for this preprint (which was not certified by peer review) is the author/funder, who has granted bioRxiv a license to display the preprint in perpetuity. It is made available under aCC-BY 4.0 International license.

no divisions were observed beyond this distance (**Figure 2**). Finally, cells were assigned as dying based on their ejection from the epithelium, while the remaining unassigned cells were classified as undetermined and not included in the analysis.

We tested the accuracy of this approach as follows. In data sets of >60 hours in length, we selected the subset of all cells for which we could with certainty determine proliferative state, either because they divided or because they did not divide for at least 40 hours. We then truncated these data sets to the first 40 hours, which reduced the number of cells whose proliferative state we could identify with certainty, and instead determined each cells proliferative state based on the above two criteria. When we compared this result with the ground truth obtained from the >60 hour data sets, we found that out of 619 cells, we correctly assigned 141 cells as non-proliferative and 474 as proliferative. Only 4 cells were incorrectly assigned as non-dividing, whereas they were seen to divide in the >60 hour data sets.

Estimation of significance of symmetric divisions

To estimate whether the experimentally observed fraction of sisters with symmetric division outcome could be explained by sister deciding independently to proliferate further or not, we used a bootstrapping approach. In our experimental data, we identified n=499 sister pairs, where the proliferative state of each cell was known and excluding pairs where one or both sisters died. In this subset of sisters the probability of a cell dividing was found to be p=0.79. For $N=10^5$ iterations, we randomly drew n sister pairs, which each cell having probability p to be proliferative and $1-p$ to cease proliferation. For each iteration, we then calculated the resulting symmetry fraction ϕ. This resulted in a narrow distribution of ϕ with average ± st.dev. of 0.67±0.02, well-separated from the experimentally observed value of ϕ=0.97. In particular, none of 10^5 iterations resulted in a value $\phi \geq 0.97$, leading to our estimated P-value of $P<10^{-5}$. Overall, this means that the high fraction of sisters with symmetric division outcome reflects correlations in sister cell fate.

Estimation of crypt growth rate

To estimate an effective growth rate from the time dynamics of the total cell number and number of proliferating cells N for each individual crypt, we used the 'Uniform' model as defined in the main text. Here, each generation the number of proliferating cells increases by αN, and the number of non-proliferating cells, M, changes by $(1-\alpha)N$, where α is the growth rate with $-1 \leq \alpha \leq 1$. For α sufficiently close to zero, the resulting dynamics of the number of proliferating and non-proliferating cells, N and M, is given by $\frac{dN}{dt} = \frac{\alpha}{T} N$ and $\frac{dM}{dt} = \frac{1-\alpha}{T} N$, where T is the average cell cycle duration. Solving these differential equations yields $N(t) = N(0)\exp(\frac{\alpha t}{T})$ and $U(t) = M(0) - \frac{1-\alpha}{\alpha} D(0) + \frac{D(0)}{\alpha} \exp(\frac{\alpha t}{T})$ for the total number of cells, where $U = N + M$. We then fitted $U(t)$ and $N(t)$ to the experimental data in **Figure 2A,B**, using a single value of the fitting parameter α for each crypt and the experimentally determined value of T=16.2 h.

Crypt unwrapping

At every time point the crypt axis was manually annotated in the xy plane at the z position corresponding to the center of the crypt, since tracked crypts grew perpendicularly to the objective.

bioRxiv preprint doi: https://doi.org/10.1101/2022.03.17.484731; this version posted November 17, 2022. The copyright holder for this preprint (which was not certified by peer review) is the author/funder, who has granted bioRxiv a license to display the preprint in perpetuity. It is made available under aCC-BY 4.0 International license.

Three to six points were marked along the axis, through which a spline curve $\boldsymbol{s}(r)$ was interpolated. Then, for each tracked cell i we determined its position along the spline by finding the value of r that minimized the distance d between the cell position $\boldsymbol{x}_i$and the spline, i.e. $d(r_i) = \min_{\mathrm{r}} |\boldsymbol{s}(r) - \boldsymbol{x}_i|$. At each time point, the bottom-most cell of the crypt, i.e. that with the lowest value of r_i, was defined as position zero. Thus, the position along the axis p_i for cell i was defined as $p_i = r_i - \min_i(r_i)$. To determine the angle around the axis θ_i for cell i, we considered a reference vector $\boldsymbol{u}$ pointing in the direction of the imaging objective, given by $\boldsymbol{u} = (0,0,-1)$, and the vector $\boldsymbol{v}_i = \boldsymbol{x}_i - \boldsymbol{s}(r_i)$ defined by the position of the cell $\boldsymbol{x}_i$ and the position of minimum distance along the spline $\boldsymbol{s}(r_i)$. Then, the angle is given by $\theta_i = \operatorname{acos}(\boldsymbol{u} \cdot \boldsymbol{v}_i / uv)$.

Distance to Paneth cells

To estimate the distance between cells we used the following approach. For each cell at each time point we found the five closest cells within a 15 µm radius, which became the edges in a graph representation of the crypt (**Figure 5-figure supplement 1**). These values were chosen because a visual inspection revealed an average nucleus size of 10 µm and an average of five neighbors per cell. This graph was then used to define the edge distance of a cell to the nearest Paneth cell. At every time point during the lifetime of that cell, the minimum number of edges required to reach the nearest Paneth cell was recorded. The edge distance is then defined as the number of edges minus one. For example, a neighbor cell of a Paneth cell (1 edge) has a distance of zero. When the edge distance of a cell to a Paneth cell varied in time, we used the mode of its distance distribution, i.e. the most frequently-occuring value, as recorded during its lifetime.

In vivo clonal tracing

All experiments were carried out in accordance with the guidelines of the animal welfare committee of the Netherlands Cancer Institute. *Lgr*5$^{\text{EGFP-ires-CreERT2}}$;R26$_{\text{LSL-tdTomato}}$ double heterozygous male and female mice (Bl6 background) were housed under standard laboratory conditions and received standard laboratory chow and water ad libitum prior to start of the experiment. 60 hours before sacrifice, mice received an intraperitoneal injection with 0.05 mg tamoxifen (Sigma, T5648; dissolved in oil) resulting in maximally 1 labeled cell per ~10 crypts. After sacrifice, the distal small intestine was isolated, cleaned and flushed with ice cold PBSO, pinned flat and fixed for 1.5 hours in 4% PFA (7.4 pH) at 4°C. The intestine was washed in PBT (1% Tween-20) for 10 min at 4°C after which it was cut into pieces of ~2 cm and transferred to a 12 well plate for staining. The pieces were permeabilized for 5 hours in 3% BSA and 0.8% Triton X-100 in PBSO and stained overnight at 4°C using anti-RFP (Rockland, 600-401-379) and anti-GFP (Abcam, ab6673) antibodies. After 3 times 30 min washes at 4°C in 0.1% Triton X-100 and 0.2% BSA in PBSO, the pieces were incubated with Alexa fluor Donkey anti rabbit 568 (Invitrogen, A10042) and Alexa fluor Donkey anti goat 488 (Invitrogen, A11055) secondary antibodies overnight at 4°C. After an overnight wash in PBT, the pieces were incubated with DAPI (Thermo Fisher Scientific, D1306) for 2 hour and subsequently washed in PBS for 1 hour at 4°C. Next, the intestinal pieces were cleared using 'fast light-microscopic analysis of antibody-stained whole organs' (FLASH) described in Messal et al.[18]. In short, samples were moved to an embedding cassette and dehydrated in 30%, 75%, 2x 100% MetOH for 30 min each at RT. Subsequently, samples were put into MetOH in a glass dish and immersed in methyl salicylate diluted in MetOH: 25%, 75%, 2x 100% methyl salicylate (Sigma-Aldrich) 30 min each at RT protected from light. Samples were mounted in methyl salicylate in between two glass coverslips and images were

bioRxiv preprint doi: https://doi.org/10.1101/2022.03.17.484731; this version posted November 17, 2022. The copyright holder for this preprint (which was not certified by peer review) is the author/funder, who has granted bioRxiv a license to display the preprint in perpetuity. It is made available under aCC-BY 4.0 International license.

recorded using an inverted Leica TCS SP8 confocal microscope. All images were collected in 12 bit with 25X water immersion objective (HC FLUOTAR L N.A. 0.95 W VISIR 0.17 FWD 2.4 mm). Image analysis was carried out independently by two persons. Afterwards, all discrepancies between both datasets were inspected, resulting in a single dataset. Each biologically stained cell was annotated once in the 3D-dimensional image. Different cells in the same crypt were marked as belonging to the same crypt, which is necessary to calculate the clone size for that crypt. Only crypts that were fully visible within the microscopy images were analyzed.

Uncertainty estimation in clone size distributions

In organoids, the clone sizes are measured by calculating the number of offspring the cell will have 40 hours later. This calculation is performed for every hour of the time lapse, up to 40 hours before the end. *In vivo*, clone sizes are measured once per crypt, as we cannot view the dynamics over time. To estimate the uncertainty in our clone size distribution, both in organoids and *in vivo*, we use a bootstrapping approach. We denote the total number of clones observed as *N*. We then used random resampling with replacement, by drawing *N* times a random clone from the data set of observed clones, to construct a new clone size distribution. We ran this procedure 100 times, each run storing the measured fraction of clones sizes. As a result, for every clone size we obtained a distribution of fractions, which we used to calculated the standard deviation of the fraction, as a measure of sampling error.

Computational model

Simulations were initialized by generating a collection of proliferating cells, each belonging to either the niche or differentiation compartment. For each parameter combination, the initial number of proliferating cells assigned to each compartment was obtained by rounding to the closest integer the values given by the equations for N_n and N_d in the main text. When the initial number of proliferating cells in the niche compartment was lower than the compartment size S, they were randomly distributed over the compartment, with the remaining positions taken up by non-proliferating cells in order to fill the compartment. Each proliferating cell c that was generated was assigned a current age A_c and a cell cycle time C_c, i.e. the age at which the cell will eventually divide. The current age was obtained by randomly drawing a number from an interval ranging from 0 hours to the mean cell cycle time obtained from experimental data, while the cell cycle was obtained by drawing a random number from a skew normal distribution, which was fitted to the experimental distribution of cell cycle times as shown in **Figure 3-figure supplement 1**.

Simulations were performed by iterating the following routine over time, until a total simulation time $T_{sim} = 10^6$ h was reached. At each iteration i, we found the cell c_i that was due to divide next, and a time step Δt_i was defined by the time remaining for this cell to divide, i.e. $\Delta t_i = \min_c(C_c - A_c)$. Then, the ages of all proliferating cells were updated and the division of cell c_i was executed. This was done by randomly choosing one of the three division modes defined in **Figure 4C**, according to the probabilities determined by the parameters α and ϕ of the compartment to which the cell belonged. Any proliferating daughters that were born were initialized with age zero and a random cell cycle time drawn. For the two-compartment model, if the proliferating cell belonged to the niche compartment, the distalmost cell within this compartment was transferred to the differentiation compartment, without changes to its proliferative state. This means that a proliferating cell that is

bioRxiv preprint doi: https://doi.org/10.1101/2022.03.17.484731; this version posted November 17, 2022. The copyright holder for this preprint (which was not certified by peer review) is the author/funder, who has granted bioRxiv a license to display the preprint in perpetuity. It is made available under aCC-BY 4.0 International license.

transferred to the differentiation compartment will still divide, with the symmetry only determined by ϕ, even if α_d=-1, i.e. all divisions in the differentiation compartment generate non-proliferating daughters. This corresponds to the assumption that the decision to proliferate or not, as well as the symmetry between the resulting daughters, is set by the external environment (niche or differentiation compartments) the cell experiences at birth and cannot be reversed at a later point. Finally, the number of proliferating and non-proliferating cells in each compartment was updated accordingly. Cell rearrangements were implemented as follows. For each iteration i, with time step Δt_i, we drew the number of cell rearrangements from a Poisson distribution with mean $(r \cdot S)\Delta t_i$, where r is the rearrangement rate per cell. We then implemented each individual rearrangement by randomly selecting a cell at position $j \in (0, S\text{-}1)$ and swapping it with the cell at position j+1.

The model had six parameters, of which three $(\alpha_n, \alpha_d, \phi)$ were systematically varied in our simulations. The remaining parameters were constrained by the experiments. We picked the niche size S so that the total number of proliferating cells was 30, corresponding to the typical number of dividing cells observed in the experiments, through a procedure outline in the main text. We obtained the average cell cycle duration T, as well as its distribution, from the data in **Figure 3-figure supplement 1**. Finally, we obtained the rearrangement rate r from the observed (a)symmetry in proliferative fate observed between cousin cells. For a 'well-mixed' niche compartment, $r{\cdot}T{\gg}1$, cousin pairs showed asymmetric outcome as often as symmetric outcome (**Figure 4-figure supplement 2**), in contrast to our experimental observations (**Figure 3A**). In contrast, for infrequent cell rearrangement, $r{\cdot}T{=}1$, cells expelled from this compartment close together in time are also closely related by lineage, leading to correlations in division outcome between cousins that reproduced those observed experimentally (**Figure 4-figure supplement 2, Figure 3A**).

For some parameter values, simulations were ended earlier than the total time T_{sim}. This occurred when no proliferating cells were left in either compartment (defined as a depletion event), or when the number of proliferating cells reached an arbitrarily set maximum limit of five times its initial value (defined as an overgrowth event, occurring only in the one-compartment model). In these cases, simulations were restarted until a total simulation time T_{sim} was reached, and the total number of events was recorded. Thus, the rate of depletion or overgrowth refers to the number of times simulations had to be restarted for each value of ϕ divided by the total simulation time.

To obtain statistics regarding fluctuations on the number of proliferating cells N through time, at each iteration i we kept track of the number of proliferating cells in the niche compartment d_i^p and in the differentiation compartment d_i^n. With these quantities, we could compute the standard deviation σ of N according to $\sigma^2 = \langle N^2 \rangle - \langle N \rangle^2$. Given that $N = N_n + N_d$, where N_n and N_d are the number of proliferating cells in the niche and differentiation compartments, σ can be expressed as $\sigma^2 = \langle N_n^2 \rangle - \langle N_n \rangle^2 + \langle N_d^2 \rangle - \langle N_d \rangle^2 + 2\langle N_n N_d \rangle - 2\langle N_n \rangle \langle N_d \rangle$, where $\langle N_{n,d} \rangle = \sum_i \frac{d_i^{n,d} \Delta t_i}{T}$, $\langle N_{n,d}^2 \rangle = \sum_i \frac{\left(d_i^{n,d}\right)^2 \Delta t_i}{T}$ and $\langle N_n N_d \rangle = \sum_i \frac{d_i^n d_i^d \Delta t_i}{T}$.

Code and data availability

All cell lineage data, simulation code and data analysis scripts used to generate the figures have been deposited in Zenodo under accession codes 10.5281/zenodo.7197573.

bioRxiv preprint doi: https://doi.org/10.1101/2022.03.17.484731; this version posted November 17, 2022. The copyright holder for this preprint (which was not certified by peer review) is the author/funder, who has granted bioRxiv a license to display the preprint in perpetuity. It is made available under aCC-BY 4.0 International license.

bioRxiv preprint doi: https://doi.org/10.1101/2022.03.17.484731; this version posted November 17, 2022. The copyright holder for this preprint (which was not certified by peer review) is the author/funder, who has granted bioRxiv a license to display the preprint in perpetuity. It is made available under aCC-BY 4.0 International license.

References

1. Simons, B.D. and H. Clevers, *Strategies for homeostatic stem cell self-renewal in adult tissues.* Cell, 2011. **145**(6): p. 851-62.
2. Lander, A.D., et al., *Cell lineages and the logic of proliferative control.* PLoS Biol, 2009. **7**(1): p. e15.
3. Clayton, E., et al., *A single type of progenitor cell maintains normal epidermis.* Nature, 2007. **446**(7132): p. 185-9.
4. Klein, A.M., et al., *Kinetics of cell division in epidermal maintenance.* Phys Rev E Stat Nonlin Soft Matter Phys, 2007. **76**(2 Pt 1): p. 021910.
5. Klein, A.M. and B.D. Simons, *Universal patterns of stem cell fate in cycling adult tissues.* Development, 2011. **138**(15): p. 3103-11.
6. Lopez-Garcia, C., et al., *Intestinal stem cell replacement follows a pattern of neutral drift.* Science, 2010. **330**(6005): p. 822-5.
7. Rué, P. and A. Martinez Arias, *Cell dynamics and gene expression control in tissue homeostasis and development.* Mol Syst Biol, 2015. **11**(1): p. 792.
8. Feller, W., *Die grundlagen der volterraschen theorie des kampfes ums dasein in wahrscheinlichkeitstheoretischer behandlung.* Acta Biotheoretica, 1939. **5**(1): p. 11-40.
9. Sun, Z. and N.L. Komarova, *Stochastic modeling of stem-cell dynamics with control.* Mathematical biosciences, 2012. **240**(2): p. 231-240.
10. Gehart, H. and H. Clevers, *Tales from the crypt: new insights into intestinal stem cells.* Nat Rev Gastroenterol Hepatol, 2019. **16**(1): p. 19-34.
11. Farin, H.F., J.H. Van Es, and H. Clevers, *Redundant sources of Wnt regulate intestinal stem cells and promote formation of Paneth cells.* Gastroenterology, 2012. **143**(6): p. 1518-1529.e7.
12. Sato, T., et al., *Paneth cells constitute the niche for Lgr5 stem cells in intestinal crypts.* Nature, 2011. **469**(7330): p. 415-8.
13. Shoshkes-Carmel, M., et al., *Subepithelial telocytes are an important source of Wnts that supports intestinal crypts.* Nature, 2018. **557**(7704): p. 242-246.
14. Scoville, D.H., et al., *Current view: intestinal stem cells and signaling.* 2008. **134**(3): p. 849-864.
15. Winton, D. and B. Ponder, *Stem-cell organization in mouse small intestine.* Proceedings of the Royal Society of London. Series B: Biological Sciences, 1990. **241**(1300): p. 13-18.
16. Snippert, H.J., et al., *Intestinal crypt homeostasis results from neutral competition between symmetrically dividing Lgr5 stem cells.* Cell, 2010. **143**(1): p. 134-44.
17. Ritsma, L., et al., *Intestinal crypt homeostasis revealed at single-stem-cell level by in vivo live imaging.* Nature, 2014. **507**(7492): p. 362-365.
18. Sato, T., et al., *Single Lgr5 stem cells build crypt-villus structures in vitro without a mesenchymal niche.* 2009. **459**(7244): p. 262-265.
19. Doupé, D.P., et al., *A single progenitor population switches behavior to maintain and repair esophageal epithelium.* Science, 2012. **337**(6098): p. 1091-3.
20. Klein, A.M., et al., *Mouse germ line stem cells undergo rapid and stochastic turnover.* Cell Stem Cell, 2010. **7**(2): p. 214-24.
21. Teixeira, V.H., et al., *Stochastic homeostasis in human airway epithelium is achieved by neutral competition of basal cell progenitors.* Elife, 2013. **2**: p. e00966.
22. Ragkousi, K. and M.C. Gibson, *Cell division and the maintenance of epithelial order.* J Cell Biol, 2014. **207**(2): p. 181-8.
23. Kok, R.N.U. and J.S. van Zon, OrganoidTracker, Github, https://github.com/jvzonlab/OrganoidTracker/tree/v1. c97816d
24. Swain, P.S., *Lecture notes on stochastic models in systems biology.* arXiv preprint arXiv:1607.07806, 2016.

bioRxiv preprint doi: https://doi.org/10.1101/2022.03.17.484731; this version posted November 17, 2022. The copyright holder for this preprint (which was not certified by peer review) is the author/funder, who has granted bioRxiv a license to display the preprint in perpetuity. It is made available under aCC-BY 4.0 International license.

25. Corominas-Murtra, B., et al., *Stem cell lineage survival as a noisy competition for niche access.* Proc Natl Acad Sci U S A, 2020. **117**(29): p. 16969-16975.
26. Kok, R.N.U., S.J. Tans, and J.S. van Zon, *Minimizing cell number fluctuations in self-renewing tissues with a stem cell niche.* bioRxiv, 2022: p. 2022.03.10.483777.
27. Farin, H.F., et al., *Visualization of a short-range Wnt gradient in the intestinal stem-cell niche.* Nature, 2016. **530**(7590): p. 340-3.
28. Langlands, A.J., et al., *Paneth Cell-Rich Regions Separated by a Cluster of Lgr5+ Cells Initiate Crypt Fission in the Intestinal Stem Cell Niche.* PLoS Biol, 2016. **14**(6): p. e1002491.
29. Itzkovitz, S., et al., *Optimality in the development of intestinal crypts.* Cell, 2012. **148**(3): p. 608-19.
30. Sei, Y., et al., *Asymmetric cell division-dominant neutral drift model for normal intestinal stem cell homeostasis.* 2019. **316**(1): p. G64-G74.
31. Eisenhoffer, G.T. and J. Rosenblatt, *Bringing balance by force: live cell extrusion controls epithelial cell numbers.* Trends Cell Biol, 2013. **23**(4): p. 185-92.
32. Li, L. and T. Xie, *Stem cell niche: structure and function.* Annu Rev Cell Dev Biol, 2005. **21**: p. 605-31.

bioRxiv preprint doi: https://doi.org/10.1101/2022.03.17.484731; this version posted November 17, 2022. The copyright holder for this preprint (which was not certified by peer review) is the author/funder, who has granted bioRxiv a license to display the preprint in perpetuity. It is made available under aCC-BY 4.0 International license.

Supporting Figures

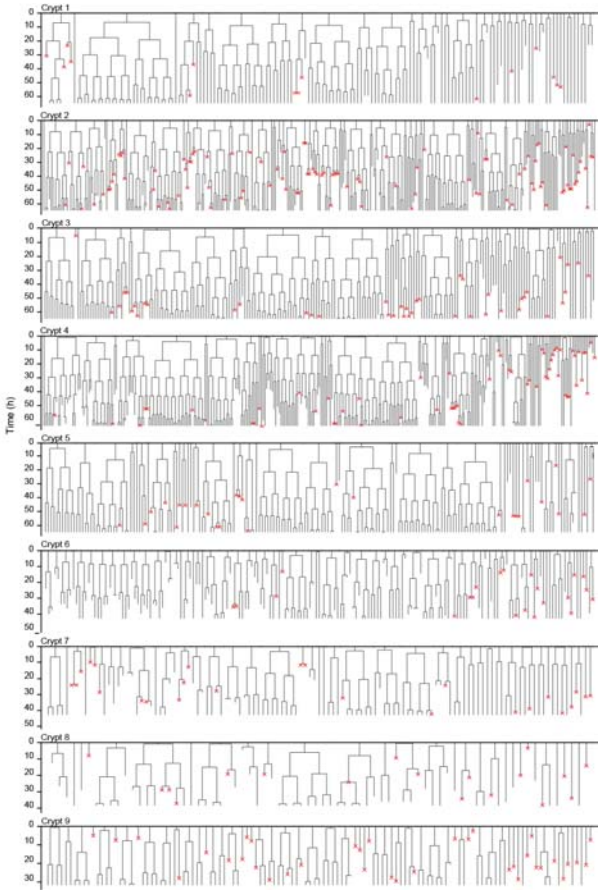

Figure 1–figure supplement 1. Lineage trees of all tracked cells

Lineage trees of cells tracked in nine different crypts. Cells in the initial time point are ordered according to their distance to the crypt base. Red crosses indicate cell deaths and incomplete lines indicate cells that could not be accurately traced further due to insufficient fluorescence intensity or movement outside of the field of view.

bioRxiv preprint doi: https://doi.org/10.1101/2022.03.17.484731; this version posted November 17, 2022. The copyright holder for this preprint (which was not certified by peer review) is the author/funder, who has granted bioRxiv a license to display the preprint in perpetuity. It is made available under aCC-BY 4.0 International license.

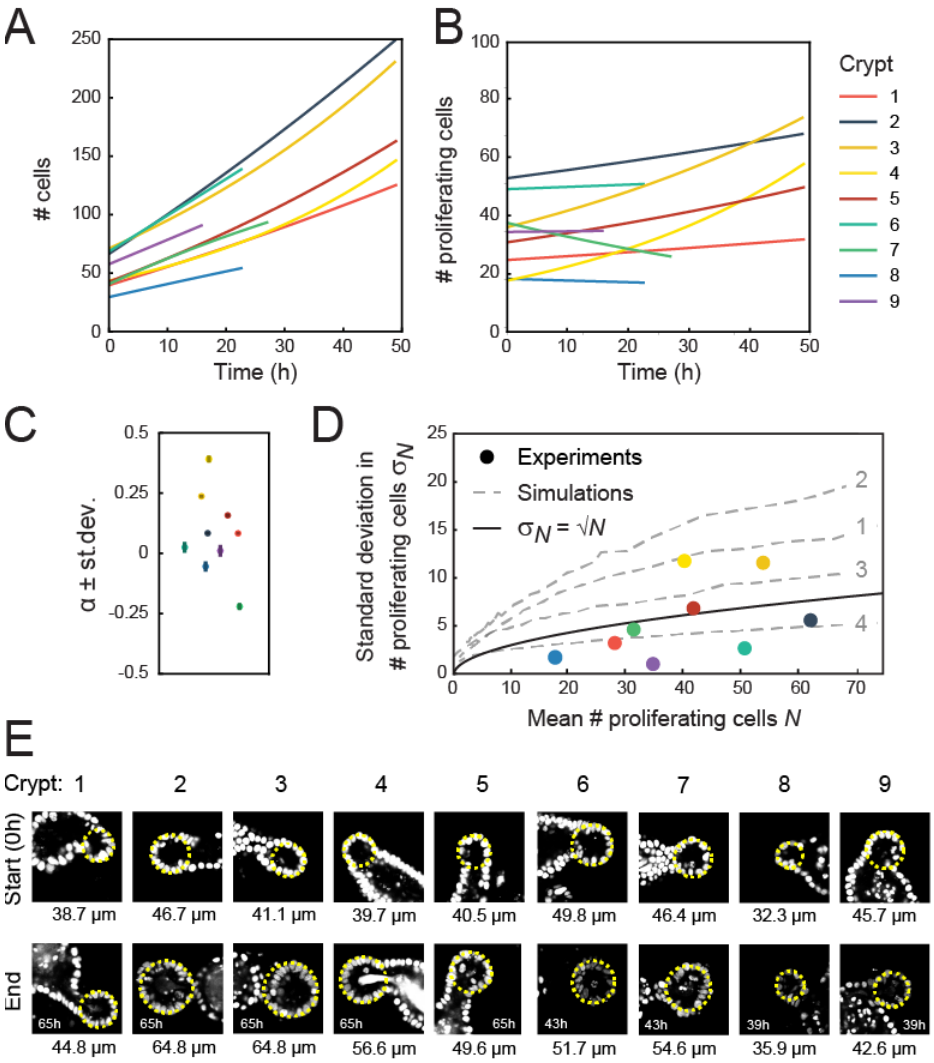

Figure 2–figure supplement 1. Crypt growth and heterogeneity

(A),(B) Fits of a simple cell proliferation model (**Materials and Methods**) to the experimental data in **Figure 2A,B**. Each fit to the total number of cells (A) and number of proliferating cells (B) yields a single fitted value of the exponential growth rate α. **(C)** Fitted values of α, with the color of each marker corresponding to the crypts in (A),(B). Two crypts exhibited significant growth (crypts 3 and 4, α≥0.25) while one crypt show decay in proliferating cell number (crypt 7, α=-0.25). For most of the remaining crypts, α deviated significantly from zero, but otherwise the fitted growth was low. For this reason, the reported average growth rate in the main text excluded crypts 3,4 and 7. Including crypt 7 yields $\alpha=0.0\pm0.1$. Error bars are the standard deviation in the fit of α. **(D)** Standard deviation of the number of proliferating cells, σ_D, versus the average, D, for each crypt, with color indicating crypts as in (A),(B). Black line shows the relationship expected for a Poisson birth-death process, $\sigma_D=\sqrt{D}$. For crypts that exhibited growth (crypt 3 and 4), σ_D was larger than a Poisson process, while other crypts showed fluctuations close to or below what was expect for a Poisson process, implying that fluctuations were limited by some form of homeostatic control. Grey dashed lines show the same analysis for simulations of the 'Compartment' model (**Figure 4D**), with individuals lines

bioRxiv preprint doi: https://doi.org/10.1101/2022.03.17.484731; this version posted November 17, 2022. The copyright holder for this preprint (which was not certified by peer review) is the author/funder, who has granted bioRxiv a license to display the preprint in perpetuity. It is made available under aCC-BY 4.0 International license.

corresponding to the different scenarios 1-4 (indicated in grey) in **Figure 4E,F**. For the suboptimal scenarios 1-3, fluctuations are larger than Poissonian, while the optimal scenario 4 reproduced the low fluctuations observed experimentally. **(E)** Fluorescence images of analyzed crypts 1-9 at the start and end of the experiment. Duration of the experiment is indicated in each 'end' panel. Diameter of the crypt at the start and end of the experiment is calculated by overlaying a circle (yellow line) over the z-slice at the center of the crypt. Overall, crypts display heterogeneity both in initial crypt size and growth of crypt diameter.

bioRxiv preprint doi: https://doi.org/10.1101/2022.03.17.484731; this version posted November 17, 2022. The copyright holder for this preprint (which was not certified by peer review) is the author/funder, who has granted bioRxiv a license to display the preprint in perpetuity. It is made available under aCC-BY 4.0 International license.

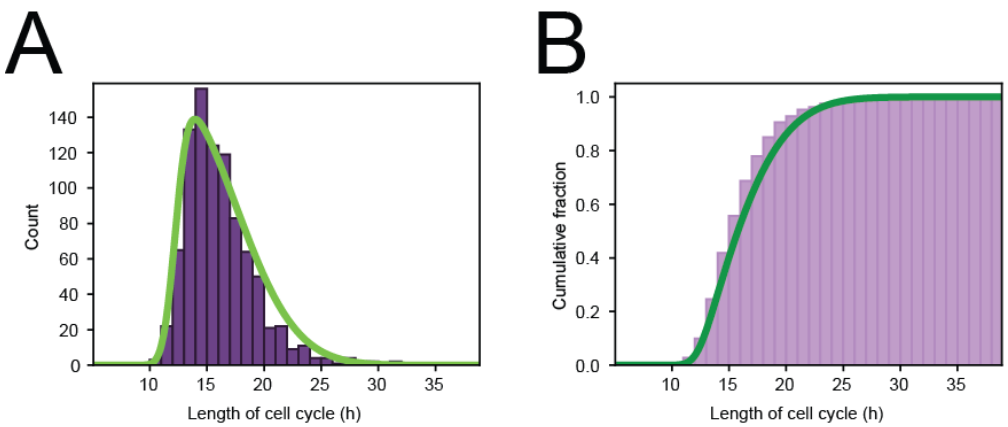

Figure 3-figure supplement 1. Cell cycle distribution

(A) Histogram of cell cycle times of all tracked dividing cells. Green line represents a skew normal distribution fitted to the data, with parameters: shape = 6.1, location = 12.2 h, and scale = 5.2 h. **(B)** Cumulative version of the histogram of panel (A).

bioRxiv preprint doi: https://doi.org/10.1101/2022.03.17.484731; this version posted November 17, 2022. The copyright holder for this preprint (which was not certified by peer review) is the author/funder, who has granted bioRxiv a license to display the preprint in perpetuity. It is made available under aCC-BY 4.0 International license.

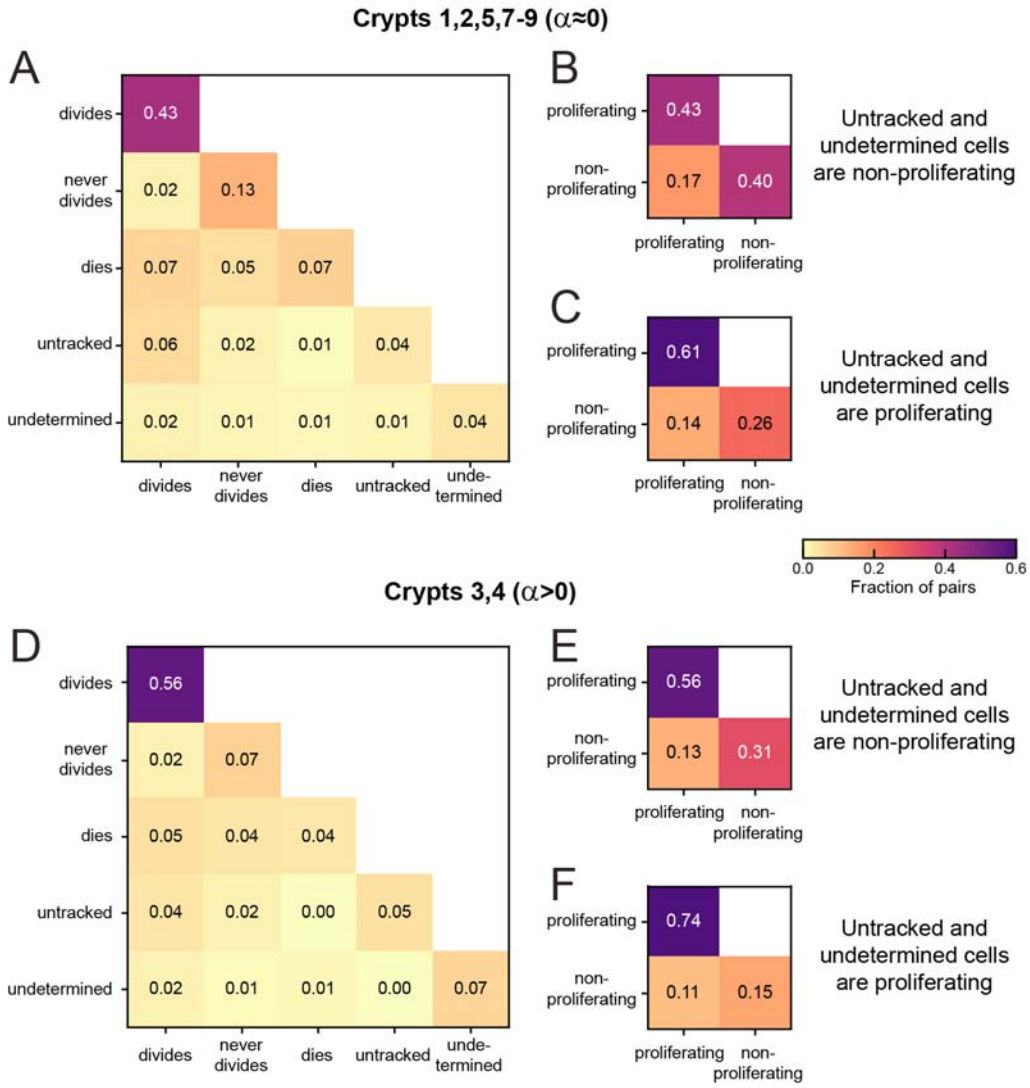

Figure 3-figure supplement 2. Sister pair divisions patterns and proliferation control.

(A) Correlations in division patterns between sister pairs (S_1,S_2), for all cells born at least 15 h prior to the end of the experiment in crypts that exhibited low growth rate $\alpha \approx 0$ in **Figure 2-figure supplement 1B,C** (Crypts 1,2,5,7-9). Sister pair fractions are also included for cells that were lost from cell tracking (untracked) or cells that could be tracked but where the experiment ended before a division could be observed or excluded (undetermined). **(B)** Fraction of sister pairs with proliferating and/or non-proliferating cells, under the assumption that untracked and undetermined cells are non-proliferating. This assumption matches our observation that untracked cells are located almost exclusively in the villus, where cells are less likely to proliferate, and that undetermined cells older than 15 h are most likely non-proliferating according to **figure 3-figure supplement 1**. Cells that died were classified as non-proliferating, as in **Figure 2A,B**. Under this assumption, the fraction of symmetrically proliferating (43%) and non-proliferating sisters (40%) is approximately equal, consistent with constant number of proliferating cells and low growth rate α in **Figure 2A,B** and **Figure 2-figure supplement 1B,C**. **(C)** Fraction of sister pairs with proliferating and/or non-proliferating cells, under the assumption that all untracked and undetermined cells proliferate. Under this assumption, which is not supported by our experiments, the fraction of symmetrically

bioRxiv preprint doi: https://doi.org/10.1101/2022.03.17.484731; this version posted November 17, 2022. The copyright holder for this preprint (which was not certified by peer review) is the author/funder, who has granted bioRxiv a license to display the preprint in perpetuity. It is made available under aCC-BY 4.0 International license.

proliferating (61%) and non-proliferating sisters (26%) is still relatively close to balanced, implying that the balance in proliferation observed in (B) is likely not impacted strongly if a small fraction of untracked or undetermined cells would have been proliferating. **(D)** Same as (A) but for crypts that exhibited an increase in number of proliferating cells ($\alpha>0$, Crypts 3,4). **(E)**,**(F)** Same as (B),(C) but for Crypts 3 and 4. Symmetrically proliferating sisters (56%) outnumber non-proliferating sisters (31%) even under the assumption that all untracked and undetermined sisters are non-proliferating, consistent with the growth in proliferating cells observed in these crypts.

bioRxiv preprint doi: https://doi.org/10.1101/2022.03.17.484731; this version posted November 17, 2022. The copyright holder for this preprint (which was not certified by peer review) is the author/funder, who has granted bioRxiv a license to display the preprint in perpetuity. It is made available under aCC-BY 4.0 International license.

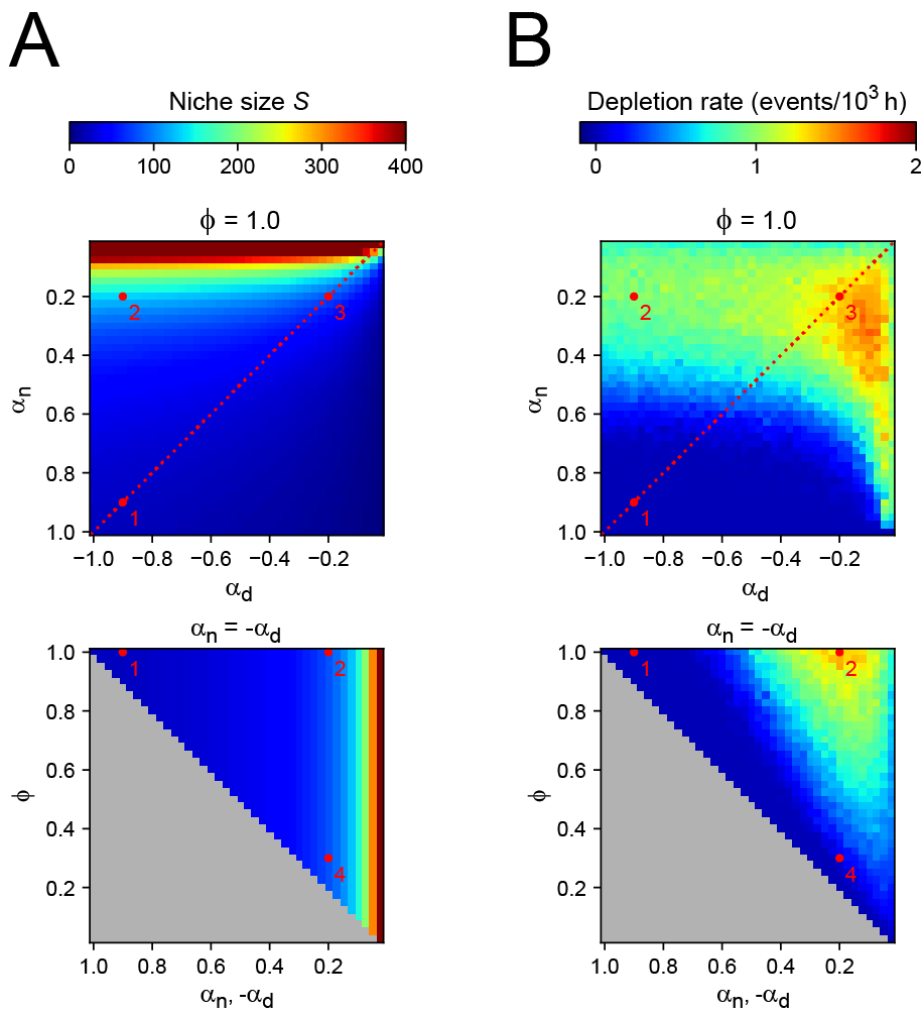

Figure 4-figure supplement 1. Two-compartment model

(A) Number of cells S in the niche compartment, as function of model parameters in the Compartment model. Top panel shows the effects of varying the bias towards proliferative daughters of the niche and differentiation compartments (α_n and α_d, respectively) when all divisions are symmetric ($\phi = 1$), and bottom panel shows the effects of varying the degree of symmetry when these compartments have opposite growth rates ($\alpha_n = -\alpha_d$, dashed line in top panel). The grey region in bottom panel corresponds to inaccessible parameter space. Numbers correspond to the parameter sets highlighted in Figure 4 in the main text. **(B)** Rate at which proliferating cells were depleted. Every time a simulation ended due to depletion, i.e. all remaining cells are non-proliferating, a new simulation was started until a total simulation time of 10^6 hours was reached. Thus, the rate refers to the number of times simulations had to be restarted for each value of the parameters divided by the total simulation time. Spontaneous overgrowth was only observed in cases where α_p and α_n are both close to 0, in which case the rate was low ($\sim 10^{-5}$ h^{-1}).

bioRxiv preprint doi: https://doi.org/10.1101/2022.03.17.484731; this version posted November 17, 2022. The copyright holder for this preprint (which was not certified by peer review) is the author/funder, who has granted bioRxiv a license to display the preprint in perpetuity. It is made available under aCC-BY 4.0 International license.

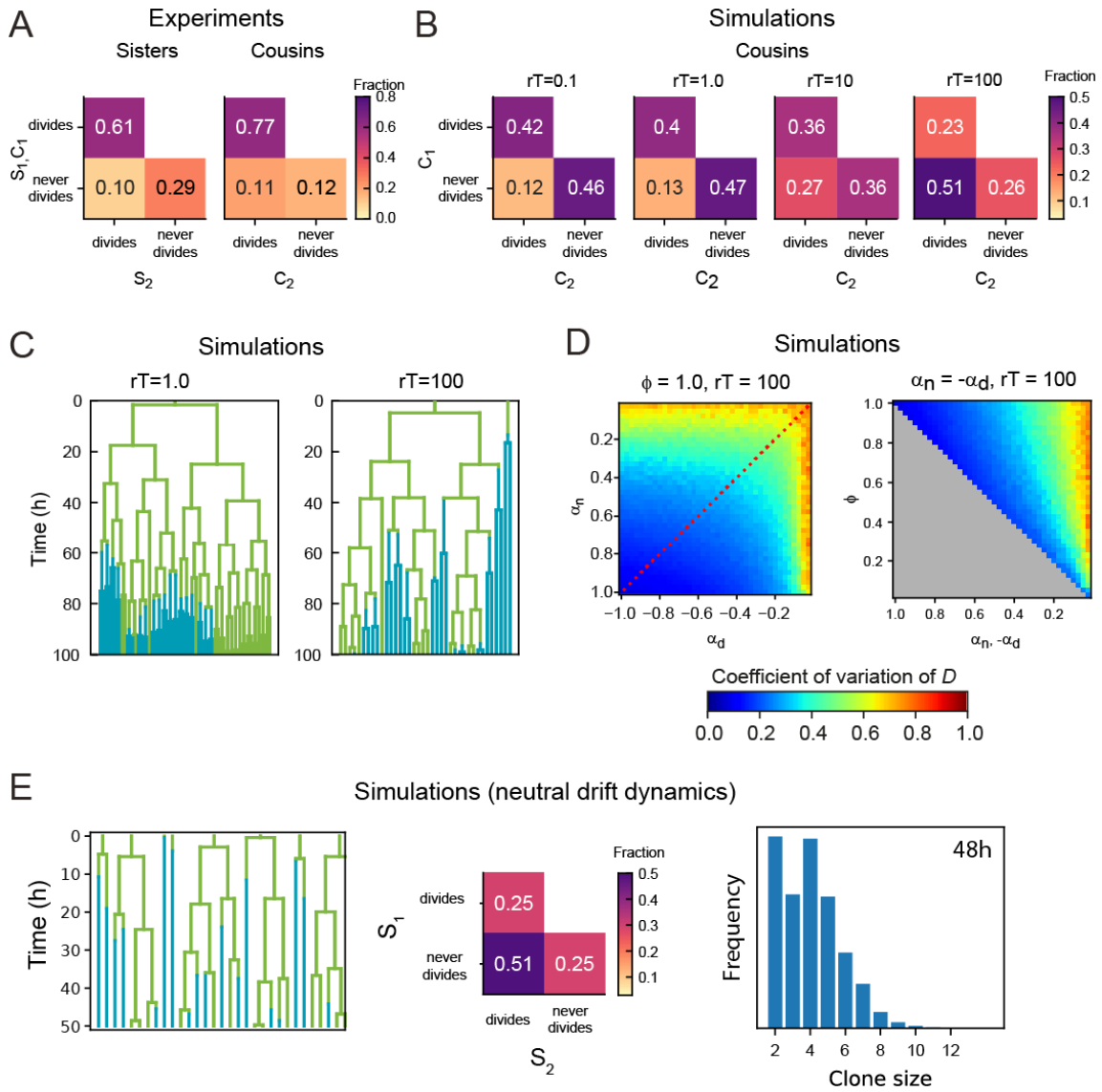

Figure 4-figure supplement 2. Dependence of lineage dynamics on cell rearrangements.

(A) Experimentally observed correlations in division patterns between sister pairs (S_1,S_2, n=499) and cousin cells pairs (C_1,C_2, n=560), for cell pairs where neither cell died. **(B)** Correlations in division pattern between cousin cells (C_1,C_2) for simulations of the two-compartment model, for increasing cell rearrangement rate r. Here, the product $r{\cdot}T$, where T is the average cell cycle duration, indicates the approximate number of rearrangements experienced per cell cycle. For a 'well-stirred' proliferative compartment, $r{\cdot}T \gg 1$, asymmetric lineage outcome is more prevalent that symmetric outcome for cousin cells. However, for infrequent cell rearrangements, $r{\cdot}T \approx 1$, asymmetric lineage outcome for cousin cells is less prevalent that symmetric outcome, with a frequency that resembles that seen experimentally in (A). Data is averaged over 50 independent simulations, with $\alpha_n = -\alpha_d = 0.95$, $\phi = 0.95$, and the average number of proliferating cells $\langle D \rangle = 30$. **(C)** Example lineage trees obtained from simulations for different $r{\cdot}T$. Line color indicates whether the cell was in the proliferative (green) or non-proliferative compartment (blue). For $r{\cdot}T = 1$, closely related cells remain largely together in space, causing ejections from the proliferative compartment to be

bioRxiv preprint doi: https://doi.org/10.1101/2022.03.17.484731; this version posted November 17, 2022. The copyright holder for this preprint (which was not certified by peer review) is the author/funder, who has granted bioRxiv a license to display the preprint in perpetuity. It is made available under aCC-BY 4.0 International license.

correlated within lineages. As a consequence, not only sisters, but also cousins and more distantly related cells keep proliferating or cease proliferation together. For $r{\cdot}T = 100$, this correlation within lineage trees is lost. **(D)** Coefficient of variation of the total number of proliferating cells D for simulations with a 'well-stirred' proliferative compartment, $r{\cdot}T$=100. Left panel shows the effects of varying the growth rates of both compartments when all divisions are symmetric and right panel of varying the degree of symmetry when both compartments have opposite growth rates. Overall, the coefficient of variation shows a similar dependence on parameters as seen for the simulations with infrequent cell rearrangements, $r{\cdot}T = 1$, shown in Figure 4 in the main text. **(E)** Simulations of a neutral drift dynamics model for $N = 30$. This model is similar to the 'well-stirred' two-compartment model for the case where all cells are proliferative in the niche compartment ($\alpha_n = 1$, $\phi = 1$), and no cells are proliferative in the differentiation compartment ($\alpha_n = -1$, $\phi = 1$). However, the main difference is that in the neutral drift model, cells switch from proliferative to non-proliferative immediately upon exiting the niche compartment. This results in half of all divisions being asymmetric, as every cell has an independent chance of 50% to exit the niche and thus halt proliferation.

bioRxiv preprint doi: https://doi.org/10.1101/2022.03.17.484731; this version posted November 17, 2022. The copyright holder for this preprint (which was not certified by peer review) is the author/funder, who has granted bioRxiv a license to display the preprint in perpetuity. It is made available under aCC-BY 4.0 International license.

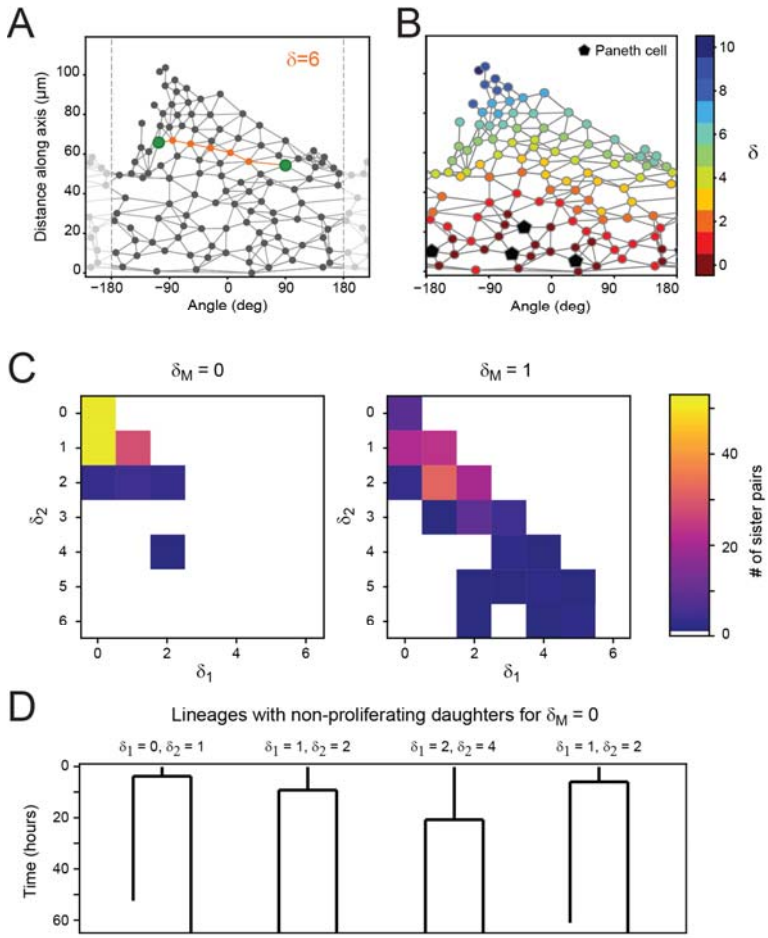

Figure 5-figure supplement 1. Proliferation dynamics as function of Paneth cell distance.

(A) After crypt unwrapping and determination of neighbors, the link distance δ between two cells (green markers) is defined as the number of edges that constitute the shortest path connecting the two cells (indicated in orange, resulting in this case in a neighbor distance of δ=6. **(B)** Link distance δ of each cell to its closest Paneth cell, shown for a single time point. **(C)** Distribution of Paneth cell distances δ_1 and δ_2 of sister pairs generate from a mother cell either directly touching a Paneth cell (δ_M=0) or one cell removed from a Paneth cell (δ_M=1). **(D)** Examples of cell lineages for rare sister pairs that ceased proliferation, even though their mother was touching a Paneth cell (δ_M=0). For each sister pair, the distances δ_1 and δ_2 after division are given.